Journal of Energy Storage 55 (2022) 105440

Contents lists available at ScienceDirect

Journal of Energy Storage

journal homepage: www.elsevier.com/locate/est

Research Papers

The nonlinearities in the galvanostatic charging curves of supercapacitors provide insights into charging mechanisms

L.E. Helseth

Department of Physics and Technology, Allegaten 55, 5020 Bergen, University of Bergen, Norway

ARTICLE INFO

Keywords:
Supercapacitor
Galvanostatic charging
Energy storage

ABSTRACT

Supercapacitors are often charged using constant currents. The capacitance can be determined from the slope of the voltage-time curve if the measured voltage over the supercapacitor increases linearly with time. However, the resulting voltage-time curve is often nonlinear, which may lead one to interpret the capacitance as being either time or voltage dependent. In the current work, systematic experimental studies of the nonlinearity of galvanostatic charging curves as a function of applied current and temperature are undertaken for commercial supercapacitors in the range 1–1000 F. A consistent theory is developed to explain the available data. It is demonstrated that the nonlinearity in the voltage-time curve can be attributed to a constant capacitance in parallel with a resistance, the latter which is inversely proportional to the applied current. The influence of faradaic charge transfer reactions or surface charge reorganization on this parallel resistance is analyzed. The proposed theory is also used to analyze galvanostatic charging data available in the research literature, and the different types of nonlinearities observed provide new insight into the mechanisms occurring during charging of various types of supercapacitors.

1. Introduction

Supercapacitors utilize the surface of porous carbon structures immersed in an electrolyte to store charge [1–3]. The ability to store large amounts of ionic charges at the carbon surface result in large capacitances [4,5], and supercapacitors exceeding thousands of Farads have been available the last two decades [6]. The technological progress has allowed supercapacitors to be used in intermittent renewable energy applications [7,8], wireless technology [9–11], and industrial machinery [6,12].

Despite considerable research efforts the last ten years, the progress in transforming research on supercapacitors into commercially viable products with even higher charge storage capacities has evolved relatively slowly [12]. A considerable research focus has been put on developing electrodes that allow more charge to be stored based on improved electrolytes [13–17] or nanoporous carbon structures [18,19]. However, emphasis has also been put on improving methods for accurately determining the electrical parameters governing supercapacitors [20–25]. For example, the capacitance of a supercapacitor is often determined using the slope of galvanostatic charging/discharging curves. However, such curves are often nonlinear, which makes it challenging to extract accurate capacitance values that coincide with those obtained using other electrical techniques such as impedance spectroscopy and cyclic voltammetry [26]. From a fundamental perspective, the source of this nonlinearity is not well understood, although it has recently been attributed to factors such as for example voltage-dependent dipole orientation [27] or carbon electrode structure [28]. Transmission line circuits has been used to demonstrate how charge redistribution and electrode history influence the galvanostatic charging/discharging curves, thus providing insight into these important phenomena [29]. However, to date no theory has been constructed which consistently can be used to model these nonlinearities and to interpret the galvanostatic charging curves when parameters such as temperature and current are varied.

Different electrical techniques provide different insight into the working mechanism of a supercapacitor. While impedance spectroscopy is a perturbative technique that investigates small perturbations at a sequence of particular frequencies, cyclic voltammetry usually goes beyond small perturbations and investigates the nonlinear current following an applied voltage. As discussed in ref. [26], these techniques give different electrical information than when a constant current is applied, and care must be taken to extract reliable values for the capacitance. In addition, better methods are needed to extract more and better data from galvanostatic charging/discharging curves. In ref. [26]

E-mail address: lars.helseth@ift.uib.no.

https://doi.org/10.1016/j.est.2022.105440
Received 15 May 2022; Received in revised form 20 July 2022; Accepted 6 August 2022
Available online 12 August 2022

it was argued that galvanostatic charging curves are better suited for determining capacitance than discharging curves since the latter may depend on the initial charge state. Therefore, the current work starts with building a model for consistently interpreting galvanostatic charging curves, followed by an investigation on how to interpret them in terms of an equivalent electrical circuit. The model is then used to examine a range of experimental data, both new data reported here as well as already published data in the literature. The work presented provides a new method for extraction and interpretation of capacitance values obtained using galvanostatic charging curves which might help reveal the underlying charge transport mechanisms.

2. A model for galvanostatic charging

In this section, the currents through a supercapacitor are first discussed, followed by a formulation of suitable equivalent circuits.

2.1. The currents flowing through a supercapacitor

Fig. 1 shows a simplified schematic drawing of a supercapacitor and its operating principle. As the current flows in the electrolyte of a supercapacitor, the charge buildup on the carbon surface is given by $q_s = \sigma A$, where σ is the surface charge density (measured in C/m^2) and A is the area on which it sits. Here q_s does not participate in chemical reactions, and the entire charge is therefore associated with the electric double layer.

In addition, there is also a charge q_r which participates in redox-reactions at the surface and therefore contributes to charge transfer as faradaic reactions. Some of this charge q_r may be stored reversibly in covalent bonds in a similar manner as in a battery. If q_s is the only charge stored in a porous carbon structure, one usually calls it a supercapacitor or electrochemical double layer capacitor. Under such circumstances, the charge q_r only participates in dissipative processes and therefore does not contribute to charge storage.

However, if both q_s and q_r contribute to the charge storage, it is called a pseudocapacitor or supercapattery [30–34]. It is not always easy to separate these two types of charge storage mechanisms, which has caused quite some confusion in the research literature [30–32]. This confusion is partly due to lack of proper interpretation of experimental data, but also the fact that not all fundamental charge storage mechanisms are properly understood. For example, one normally assumes that the charge q_r does not contribute to the surface charge density [35], but that may depend on the character of the bond. For example, some oxide surfaces or polar covalent bonds may contribute to the surface charge density [36].

Here we will make the standard assumption that q_r does not contribute to the surface charge density, which is a reasonable assumption for most porous carbon surfaces that have not been heavily doped. It is then convenient to separate the two charge contributions such that the total charge is $q = q_r + q_s$, giving rise to a current given by

$$I = I_s + I_r = A\frac{d\sigma}{dt} + \sigma\frac{dA}{dt} + \frac{dq_r}{dt}. \quad (1)$$

The first term in Eq. (1) is due to a change in charge density, the second term is due to change in area on which the charge sits, while the third term is related to redox reactions. The current $I_s = dq_s/dt$ is associated with the two first terms, whereas $I_r = dq_r/dt$ is associated with the redox-reactions. While it might appear obvious that the charge density σ increases as the supercapacitor charges, it might appear to be more of a mystery why the area should change such that $dA/dt \neq 0$. However, such changes in area may occur due to several physical mechanisms. First, it has been demonstrated experimentally that intercalation or insertion of charge in the carbon structures may result in a change in size of the order of a percent [37], and that such changes are due to alterations in C—C bonds as evidenced by X-ray diffraction experiments [38]. Intercalation or insertion during galvanostatic charging is expected to create an expansion, such that $dA/dt > 0$. A second mechanism that could lead to a change in area may occur if one has spatially heterogeneous flow, and ionic charges gather in clustered patches and not like a smooth diffuse double layer as often assumed for flat surfaces. The outer ions in these clusters are obviously shielded and do not contribute to charge storage. Then, subsequent ion flow towards these regions may cause gradual or avalanche-like rearrangement of charge to cover a larger area such that in effect one has $dA/dt > 0$ during charging.

Note that Eq. (1) is an equation that only considers the currents at the porous carbon surface, and does not consider the diffusion or drift of ions in the bulk towards the surface. Transport through diffusion may play an important role in the galvanostatic charging curves in some cases, for example at low electrolyte concentrations, and will be

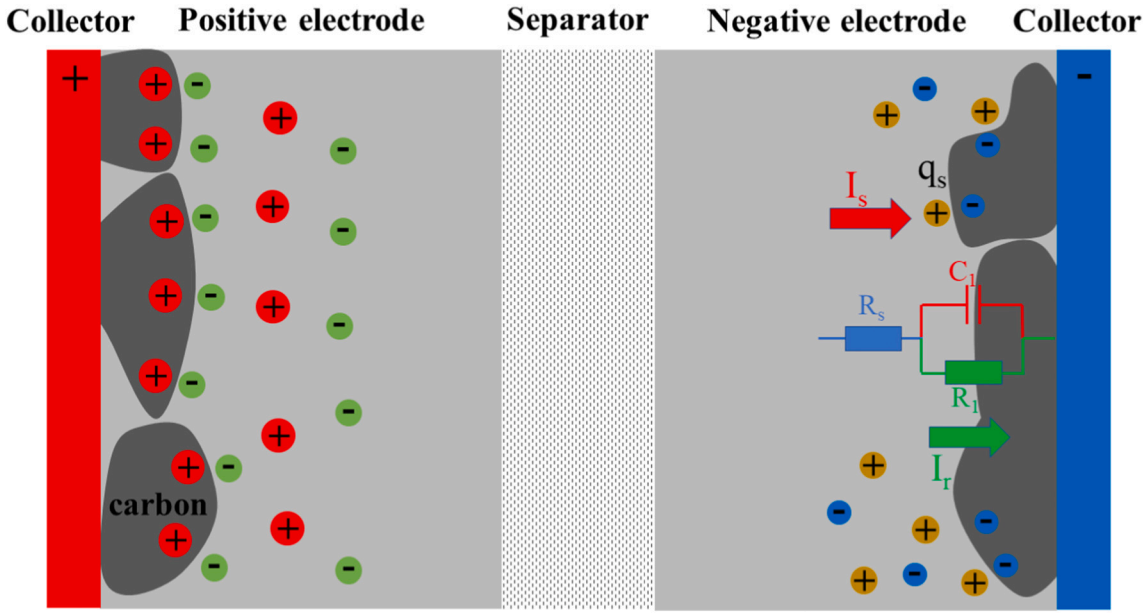

Fig. 1. Simplified schematic drawing of the structure of a supercapacitor and its operating principle. Here I_s is the capacitive charging current and I_r the charge transfer current. Also shown is an equivalent circuit with series resistor R_s, parallel-connected resistance R_1 and electrical double layer capacitance C_1.

considered in Section 8.

2.2. The surface charge density

To proceed from Eq. (1), we need a connection between the electric field and the surface charge density. In general, this is a very complex task due to the porous geometry and complex boundary conditions involved. However, one expects that they are proportional to each other, as suggested by Gauss' law. By homogenizing the porous carbon surface system and assuming a mean-field approach wherein only the electric field component in the ion flow direction perpendicular to the electrodes provides a net contribution, one may use the one-dimensional version of Gauss' law to integrate over the charge density ρ in the pores to find the effective electric field to be

$$E = \frac{1}{\varepsilon_r \varepsilon_0}\int \rho dx \approx \frac{\sigma}{\varepsilon_r \varepsilon_0}. \tag{2}$$

Here ε_r and ε_0 are the relative permittivity of the electrolyte and permittivity of vacuum, respectively. This effective field can be associated with the voltage drop V such that $E \approx V/d$, where d is a measure of the average extension of the electrical double layer at the porous surface. Thus, the arguments given here simply suggests that the surface charge density depends on the voltage according to

$$\sigma = \frac{\varepsilon_r \varepsilon_0 V}{d}. \tag{3}$$

Clearly, this simplified expression does not capture all the geometrical details of the porous structure. In fact, these have been lumped into the parameter d, which in principle may also depend on other environmental parameters. However, even though one decides to build a full three-dimensional model, it is not unreasonable to expect that the surface charge density and the applied voltage are linearly related. If this is the case, one can write

$$\sigma = \frac{C_1}{A}V, \tag{4}$$

where C_1 is the electrical double layer capacitance. In the special case where Eq. (3) is valid, one obtains $C_1 = \varepsilon_0\varepsilon_r A/d$. For cylindrical pores or other complex geometries, the capacitance takes on other geometry-dependent values. Moreover, it is technically possible that the capacitance C_1 depends on the voltage V, but this should be investigated experimentally with the proper techniques.

Inserting Eq. (3) into Eq. (1) gives

$$I = A\frac{d\sigma}{dt} + \sigma\frac{dA}{dt} + I_r = \left(\frac{\varepsilon_r\varepsilon_0 A}{d}\right)\frac{dV}{dt} + \frac{\varepsilon_r\varepsilon_0}{d}\frac{dA}{dt}V + I_r. \tag{5}$$

If one now assumes that the current is constant $I = I_0$ during charging, this equation can also be written as

$$I_0 = C_1\frac{dV}{dt} + \frac{V}{R_{ro}} + I_r, \qquad C_1 = \frac{\varepsilon_r\varepsilon_0 A}{d}, \qquad R_{ro} = \frac{1}{\frac{\varepsilon_r\varepsilon_0}{d}\frac{dA}{dt}}. \tag{6}$$

Here C_1 is the capacitance of the surface, while R_{ro} will be denoted the surface reorganization factor. The particular forms of C_1 and R_{ro} in Eq. (6) are clearly dependent of the simplifying Eq. (3) used here.

2.3. Reorganization factor

The factor $R_{ro} = d/(\varepsilon_r\varepsilon_0 dA/dt)$ is interpreted as a resistance since the term V/R_{ro} is proportional to a current in analogy with Ohm's law. If R_{ro} is due to electrolyte ion intercalation as discussed above, one may think that this term is dissipative if energy is lost as the area increases with time (i.e. $dA/dt > 0$). However, it should also be emphasized that the intercalation process could result in charge storage in addition to dissipative loss as discussed in refs. [37,38]. The area may typically not change by >0.1 %, thus rendering C_1 nearly independent of time. According to the model above, a gradual decrease in area available for charge to sit (i.e. $dA/dt < 0$) results in a negative R_{ro}, which could be interpreted as the current moving in the opposite direction due to a driving force expelling the charge from the surface. The author is not aware of direct dilatational measurements showing evidence for $dA/dt < 0$, but this does not rule out this possibility in future studies.

While the formula for surface reorganization factor $R_{ro} = d/(\varepsilon_r\varepsilon_0 dA/dt)$ depends directly on the change in area per time interval, this quantity is very hard to measure directly with existing techniques. For example, we do not know how dA/dt depends on current or temperature. To build a simple model for the condition that $dA/dt > 0$, one might imagine that the carbon surface consists of many pores and confined regions of average extension w. The ions flow into these and become trapped in a potential well. At the same time, the region expands and the charge rearranges, and the probability of escaping the potential well per unit time is $p = f_0\exp(-E/k_BT)$, where f_0 is the attempt frequency, k_B is the Boltzmann constant, T is the temperature and E the height of the potential barrier that must be surpassed for the ions to enter the confined region. In position y along the insertion channel there are N(y) ions, while at y + w there are N(y + w) ions, such that the rate of ions is $r \approx p[N(y) - N(y + w)] \approx -pwdN/dy$. The concentration of ions near each patch is $n = N/wA_c$, where A_c is a representative cross-sectional area which the ions move through while inserting. The ion flux is defined as the number of ions passing through the cross-section area A_c per unit time and is therefore $J = r/A_c \approx -D_d dn/dy$, where the diffusion coefficient is $D_d = w^2 f_0\exp(-E/k_BT)$. If one assumes normal diffusional behavior, the area covered by the ions in the potential well is proportional to that covered by diffusion, i.e. $A \propto < y^2 > \approx D_d t$ during a time t, and this can be used as a representation of the area covered during ion insertion. This means that the change in area per time is simply given by

$$\frac{dA}{dt} \propto D_d \approx w^2 f_0 e^{-\frac{E}{k_BT}} \tag{7}$$

when E = 0, the change in area per time is maximal and given by $w^2 f_0$, i.e. the area of the patches multiplied by the escape rate. One may assume that increasing the current I_0 during galvanostatic charging also increases the escape rate by pushing aside other charges on the surface, i.e. $f_0 = (N_0/e)I_0$, where k_0 is a constant and e the electronic charge $e = 1.6\bullet10^{-19}$ C. If only one ion enters per event, then $N_0 = 1$. Using this model, the surface charge reorganization factor becomes

$$R_{ro} = \frac{ede^{\frac{E}{k_BT}}}{\varepsilon_r\varepsilon_0 w^2 N_0 I_0}. \tag{8}$$

According to Eq. (8), the surface reorganization factor R_{ro} decreases inversely proportional to the current and exponentially with the temperature. Therefore, by increasing the current I_0 or the temperature T, one may expect a smaller R_{ro}.

2.4. Charge transfer resistance

In addition to the current I_s, there might also be redox-reactions resulting in charge transfer. The simplest model for this type of charge transfer follows using the Butler-Volmer equation, which states that the current due to the redox-reactions can be written as [39]

$$I_r = I_{rA}\left(e^{\alpha eV/k_BT} - e^{-(1-\alpha)eV/k_BT}\right), \tag{9}$$

where α is the transfer coefficient, $e = 1.6\bullet10^{-19}$ C is the electronic charge, $k_B = 1.38\bullet10^{-23}$ J/K and T is the temperature. The exchange current density I_{rA} depends on the surface concentration of the redox-species as well as the rate at which they are transformed, and is therefore directly proportional to the current through the supercapacitor, such that $I_{rA} = k_r I_0$, where k_r is a constant. For small voltages ($eV/k_BT << 1$) one may write

$$I_r \approx k_r I_0 \frac{eV}{k_B T} = \frac{V}{R_{ct}}, \quad R_{ct} = \frac{k_B T}{e k_r I_0}, \tag{10}$$

where R_{ct} is the charge transfer resistance. It should be noted that in Eq. (10) the charge transfer resistance decreases inversely proportional to the current, just as the surface reorganization factor in Eq. (8). However, it is also seen that R_{ro} decreases with increasing temperature, i.e., the opposite of the behavior of the charge transfer resistance in Eq. (10). The major difference between the two equations when it comes to temperature-dependence is that Eq. (8) assumes a voltage-independent energy barrier, while in Eq. (10) voltage-dependence of the energy is implicitly assumed. Under most circumstances one does not have small voltages, and the full Eq. (9) or some equivalent equation should be used to represent the redox-reaction. It is, however, convenient to keep Eq. (10) as a starting point when discussing charge transfer resistance.

The total current flowing from through the interface to the electrodes is given by $I_0 = I_s + I_r$, or

$$I_0 = C_1 \frac{dV}{dt} + \left(\frac{1}{R_{ro}} + \frac{1}{R_{ct}}\right) V \tag{11}$$

It is seen that the total resistance can be understood in terms of a parallel connection between the charge transfer resistance R_{ct} and the surface reorganization factor R_{ro}, such that the effective resistance R_1 is given by

$$\frac{1}{R_1} = \frac{1}{R_{ro}} + \frac{1}{R_{ct}}. \tag{12}$$

If $R_{ct} << R_{ro}$, it is that $R_1 \approx R_{ct}$. Under such conditions, which are achieved if $dA/dt \to 0$, the resistance is dominated by ordinary charge transfer associated with redox-reactions. On the other hand, if $R_{ct} >> R_{ro}$, it is seen that $R_1 \approx R_{ro}$. For surface reorganization to dominate one must require that $dA/dt >> edk_rI_0/(k_BT\varepsilon_r\varepsilon_0)$.

2.5. The voltage-time curve

If one defines $\tau = R_1C_1$ as the time constant for the parallel circuit consisting of R_1 and C_1, Eq. (11) is a first-order differential equation which in general can be solved to find the time-dependent voltage as

$$V(t) = I_0 \frac{\int_0^t \frac{E(t)}{C_1(t)} dt}{E(t)}, \quad E(t) = e^{\int_0^t \frac{1}{\tau(t)} dt} \tag{13}$$

Eq. (13) applies to electrochemical systems which exhibits both capacitance and loss, as detailed in Section 2.1. It does not account for non-dissipative reversible charge transfer reactions such as found in battery-like supercapacitors, but can be extended to such systems as discussed in Section 2.6. It is difficult to solve Eq. (13) for the general case where R_{ct}, A and d are time-dependent, in particular since this time-dependency is not known.

If R_1 and C_1 are time-independent, $R_1 > 0$ and $\tau = R_1C_1 > 0$, Eq. (13) results in

$$V(t) = V_0\left(1 - e^{-t/\tau}\right), \tag{14}$$

where $V_0 = R_1I_0$ is the maximum voltage.

Eq. (14) expresses the voltage across the porous carbon, and does not include any potential changes due to other parts of the supercapacitor. For example, it does not include the fact that the electrolyte itself possesses an ohmic resistance to motion of ions, the fact that there is ohmic resistance associated with the contact between the metal current collector and porous carbon surfaces, or other similar ohmic losses due to contact resistance or bulk flow. This can be done in a simple a manner, as has also been done in the literature [40], by considering the series resistance R_s as shown in Fig. 1 a). The voltage across R_s during galvanostatic charging is R_sI_0. The total voltage across the entire supercapacitor is therefore, if τ is a constant that does not depend on time, given by the simple expression

$$V_c(t) = V_0\left(1 - e^{-t/\tau}\right) + R_sI_0. \tag{15}$$

Eq. (15) will be the starting point for most of the further analysis in this work.

2.6. Electrical equivalent circuits

A number of different complex equivalent circuits have been presented to model supercapacitors [41–45]. Such equivalent circuits have been found to be very useful to model dynamic behavior [46,47], state-of-charge [48] and second-life use [49,50]. While useful in operational environments, many of these models are designed for their particular use and do not allow one to obtain further insight into the charging mechanisms. From such a perspective, the goal is to keep the electrical equivalent circuit as simple as possible with clearly defined capacitive and resistive elements that allows analysis of galvanostatic charging curves in a self-consistent manner.

The equivalent electrical circuit represented by Eq. (15) is depicted in Fig. 2 a). The equivalent circuit given in Fig. 2 a) has been considered also in previous studies [51–55], and in ref. [55] an empirical exponential relationship was proposed to explain the voltage-time curve. In the current work we investigate this further experimentally and propose that the equivalent circuit should result from the considerations leading to Eqs. (11) and (15). In Eq. (15) one obtains $dV_c(t << \tau)/dt \approx V_0/\tau$ for $t << \tau$, whereas for $t >> \tau$ it is seen that $dV_c(t >> \tau)/dt \approx 0$. It is therefore clear that the initial part of the voltage-time curve is determined by the electrical double layer capacitance C_1.

While the equivalent circuit of Fig. 2 a) does account for dissipative processes associated with faradaic reactions, it does not explicitly account for faradaic charge storage mechanisms such as observed in pseudocapacitors. The fundamentals of such mechanisms are not fully understood, and if they are not related to area change ($dA/dt \neq 0$) they are not captured by Eq. (11). It has recently been suggested that this can be done by using a charge transfer resistance R_{ct} and a faradaic capacitance C_{ct} as shown in Fig. 2 b) [35]. Assuming a constant current I_0 and $C_{ct} > 0$, the voltage across the supercapacitor represented by the equivalent circuit in Fig. 2 b) is during galvanostatic charging given by

$$V_c(t) = \frac{R_{ct}}{\left(1 + \frac{C_1}{C_{ct}}\right)^2} I_0\left(1 - e^{-t/\tau_b}\right) + R_sI_0 + \frac{I_0}{C_{ct} + C_1} t, \qquad \frac{1}{\tau_b} = \frac{1}{R_{ct}C_1} + \frac{1}{R_{ct}C_{ct}}. \tag{16}$$

Fig. 3 a) shows Eq. (16) with $R_s = 0$, $R_{ct} = 1\ \Omega$, $C_{ct} = 5C_1 = 5$ F and $I_0 = 1$ A. For $t << \tau_b$ one obtains

$$\frac{dV_c(t \ll \tau_b)}{dt} \approx \frac{I_0}{C_1}, \tag{17}$$

whereas for $t >> \tau_b$ it is seen that

$$\frac{dV_c(t \gg \tau_b)}{dt} \approx \frac{I_0}{C_{ct} + C_1} \tag{18}$$

The slope of the initial voltage-time curve is now only dependent on the capacitance C_1 of the electrical double layer, whereas the later slope depends on the combined parallel-connected double layer and charge transfer capacitances ($C_{ct} + C_1$). In Fig. 3 a) it is assumed that charge transfer capacitance C_{ct} is five times larger than the electrical double layer capacitance C_1, such that the slope at large times is six times smaller than the initial slope of the charging curve. The relative capacitance values were selected to show a possible scenario in which one would be able to detect the presence of charge transfer capacitance in a galvanostatic charging curve.

It should be pointed out that the detailed charge storage mechanism during faradaic reactions must be determined from fundamental considerations which are currently lacking. For the equivalent circuit in Fig. 2 b) to be valid it must be assumed that the faradaic current I_r

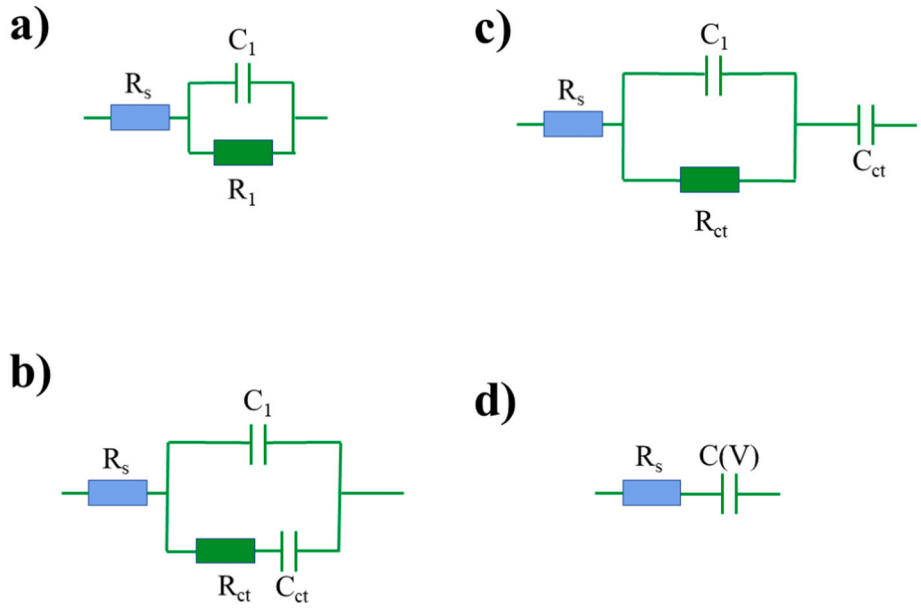

Fig. 2. Four simple models of a supercapacitor that allows one to model the nonlinearity of a galvanostatic charging curve. Here the series resistor is denoted R_s, a parallel-connected resistance R_1, the electrical double layer capacitance C_1, the charge transfer resistance R_{ct}, and the faradaic capacitance C_{ct}. In d), C(V) is a voltage-dependent capacitance.

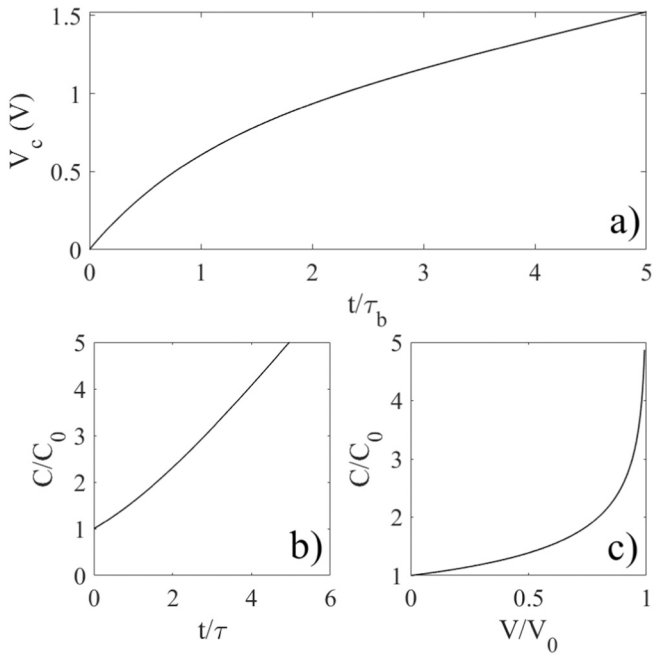

Fig. 3. In a), a plot of Eq. (16) with $R_s = 0$, $R_{ct} = 1\ \Omega$, $C_{ct} = 5C_1 = 5$ F and $I_0 = 1$ A is shown. In b), capacitance as given by Eq. (22) is shown as a function of time, and in c) the same capacitance is shown as a function of voltage.

dissipates energy as it passes through R_{ct} to the charge storage location associated with C_{ct}, in a manner completely independent of the surface charge q_s stored in the electrical double layer. However, from a fundamental point of view one may also expect the faradaic reaction to contribute to the surface charge density and therefore that the channel of current through R_{ct} combined with the current associated with the electrical double layer both combine to deliver charge to the capacitor C_{ct} as shown in Fig. 2 c). The voltage across the supercapacitor represented by the equivalent circuit in Fig. 2 c) is

$$V_c(t) = R_{ct}I_0\left(1 - e^{-t/\tau_c}\right) + R_sI_0 + \frac{I_0}{C_{ct}}t, \qquad \tau_c = R_{ct}C_1. \tag{19}$$

For $t << \tau_c$ one obtains

$$\frac{dV_c(t \ll \tau_c)}{dt} \approx I_0\left(\frac{1}{C_{ct}} + \frac{1}{C_1}\right), \tag{20}$$

whereas for $t >> \tau_c$ it is seen that

$$\frac{dV_c(t \gg \tau_c)}{dt} \approx \frac{I_0}{C_{ct}}. \tag{21}$$

From Eq. (21) it is seen that the slope of the voltage-time curve initially depends on the equivalent capacitance of the two series-connected capacitors C_1 and C_{ct}, whereas for larger t the slope depends only on the charge transfer capacitance C_{ct}. It is noted that Eq. (16) and Eq. (21) react to the charge transfer capacitance C_{ct} in different manners, and it might therefore be possible to separate the detailed charge storage mechanism of a pseudocapacitor using the galvanostatic charging curve.

2.7. Voltage-dependent capacitance

Voltage-dependent capacitances are often used to account for nonlinearities when modelling supercapacitors [56–60]. Complex equivalent circuits containing voltage-dependent capacitors are often used to model both galvanostatic charging and discharging [61,62]. The theory leading to Eq. (11) does not rule out voltage-dependent capacitance, but this should be assessed by comparison with experiments. To compare the electrical equivalent circuit model in Fig. 2 a) with that using a voltage-dependent capacitance, we consider only the very simplest model in Fig. 2 d), consisting of a voltage-dependent capacitance C(V) in series with a resistance R_s. In Fig. 2 d) one neglects any faradaic processes and assumes that all charge Q is stored in the electrical double layer. Let us assume that the charge on the capacitor is Q = C(V)V. The voltage-dependence is not known, but it is convenient to look for voltage-dependent capacitances that result in a voltage described by Eq. (14) over the capacitive element C(V). Since the current is constant, we know that $Q = I_0t$, such that the voltage-dependent capacitance is $C(V) = I_0t/V$. Using Eq. (14), the voltage-dependent capacitance can be written as

$$C = \frac{C_0 \frac{t}{\tau}}{1 - e^{-\frac{t}{\tau}}} = -C_0 \frac{ln\left(1 - \frac{V}{V_0}\right)}{\left(\frac{V}{V_0}\right)}, \quad (22)$$

where $C_0 = I_0\tau/V_0$.

Fig. 3 b) and c) shows the capacitance versus time or voltage according to Eq. (22). It is noted that $C/C_0 < 1.5$ when $t < \tau$ or $V < 0.6\ V_0$, and is within the time interval which is most often available for fitting to Eq. (15). It is therefore clear that the equivalent circuit in Fig. 2 d) may provide the same voltage-time curve as that of Fig. 1a). For this reason, from an operational point of view, wherein the underlying mechanisms are of less importance than how to operate the device, the equivalent circuits in Fig. 2 a) and 2 d) are equivalent if Eq. (22) is implemented. However, if one is interested in understanding and optimizing the charge storage, Fig. 2 a) allows a more detailed interpretation.

3. Experimental details

The experimental data reported in this work were obtained by applying a constant current while measuring the voltage over a supercapacitor. The temperature was controlled by inserting the supercapacitor into an iron bore (to ensure good thermal conductivity) placed on a hotplate. The temperature was measured at two different places on the surface of the supercapacitor and found to remain constant to within ±1 °C in the temperature range between 273 K and 363 K (0 °C and 90 °C). Before galvanostatic charging, the supercapacitor was first emptied through a 1 Ω resistor and then set to equilibrate to ensure that the voltage rebound after removal of the resistor was <0.04 V. The supercapacitors considered were of nominal capacitance/maximum nominal voltage a 1F/2.5 V supercap (GoldCap) denoted SC1, 10F/2.5 V (GoldCap) denoted SC2, 10F/2.7 V (Nichima) denoted SC3, 400F/2.7 V (Ioxus) denoted SC4, and finally 1000F/2.7 V (RND Components) denoted SC5. Current and voltage measurements were done with either a Gamry Ref. 600 (for currents up to 0.6 A) or a homemade setup utilizing a current source and a voltmeter for currents up to 30 A. During galvanostatic charging, the current fluctuations remained below ±0.1 mA and the voltage fluctuations below ±5 mV. Before each measurement, the supercapacitor was allowed to rest at least 1 h at the set temperature. Due to size and temperature stability limitations, galvanostatic charging at different temperatures was only done on the smaller (1 F and 10 F) supercapacitors.

An example of the measured voltage versus time at T = 293 K is shown in Fig. 4 a) for a 10 F/2.5 V Gold Cap supercapacitor under constant current $I_0 = 0.5$ A (blue line). In Fig. 4 b), the voltage is measured during charging with $I_0 = 0.01$A at T = 354 K for a 10 F Nichia supercapacitor (red line).

4. Interpretation of the experimental data

Given the experimental charging curves such as in Fig. 4, the question is now which equivalent model would provide a most useful fit if the goal is to extract as much information about charging mechanisms as possible.

First, it is clear that both the equivalent circuits in Fig. 2 b) and c) give rise to voltage-time curves that continues to grow linearly with time after time intervals exceeding all time constants. As such, Eqs. (16) and (19) only provide reasonable fits to the experimental curves in Fig. 4 if $I_0/C_{ct} << 1$. However, we also know that the commercial supercapacitors investigated in the current work utilize a porous carbon structure in organic electrolyte, thus making it unlikely that they do have a significant faradaic capacitance C_{ct}. For these reasons, it is believed that galvanostatic charging of pure supercapacitors is better described by the equivalent circuit in Fig. 2 a) represented by Eq. (15).

A method to determine the equivalent series resistance R_s from galvanostatic charging/discharging curves was given in ref. [63]. In the current work the supercapacitor started from zero charge before being exposed to a current jump to I_0, which means that the initial voltage jump is R_sI_0, from which the series resistance can be extracted. The value of R_s is usually determined with an accuracy within 10 %, determined by the precision of the measurement apparatus when recording the fast voltage jump after current is applied. After R_s was determined, the MatLab function nlinfit was used to make nonlinear fits of Eq. (15) to the experimental data with $R^2 > 0.99$. Here V_0 and τ could be found fitting Eq. (15) to the experimental data, and after that R_1 and C_1 could be extracted by using $V_0 = R_1I_0$ and $\tau = R_1C_1$. It is also possible to transform Eq. (15) into a linear function and use the least squares method, but it was not found to provide a better quality of the fit. However, care must be taken when doing nonlinear fits, since the MatLab function nlinfit also allows fitting of Eq. (15) to nearly linear curves wherein the values of R_1 become exceedingly large (and exhibits large uncertainty) while C_1 stays within the expected range. For this reason, each fit undertaken in this study is done several times with different starting values of the fitted parameters to ensure confidence in the results. It is found that the uncertainty in fitting parameters C_1 and R_1 were found to between about 5 % and 15 %.

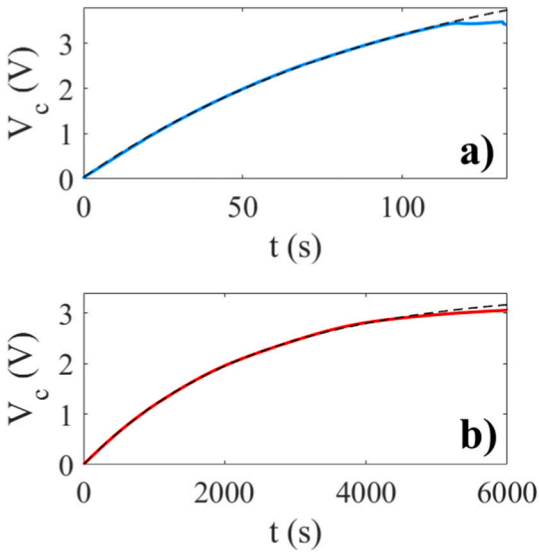

Fig. 4. In a) a 10 F/2.5 V (Gold Cap) supercapacitor denoted SC2 is charged under constant current $I_0 = 0.5$ A (blue line) at T = 293 K, whereas in b) a 10F/2.7 V (Nichima) denoted SC3 is charged at $I_0 = 0.01$ A at T = 354 K. The dashed lines are fits of Eq. (15) to the experimental data. (For interpretation of the references to colour in this figure legend, the reader is referred to the web version of this article.)

The dashed line in Fig. 4 a) is a fit of Eq. (15) to the experimental data with $U_0 = 5.2$ V, $\tau = 107$ s, $C_1 = 10.3$ F, $R_s = 74$ mΩ, whereas the dashed line Fig. 4 b) corresponds to $U_0 = 3.4$ V, $\tau = 2398$ s, $C_1 = 7.0$ F, $R_s = 97$ mΩ. It is noted that the fit of Eq. (15) to the experimental data is excellent up to about 3.2 V. For comparison, previous systematic measurements have demonstrated that porous carbon in organic electrolytes such as lithium tetrafluoroborate ($LiBF_4$) or tetraethylammonium tetrafluoroborate ($TEABF_4$) dissolved in acetonitrile or propylene carbonate all typically exhibit a stagnation in the voltage growth above 3.2 V [64]. In Ref. [64] this was assigned to a faradaic process, possibly leading to irreversible kinetics. It is possible that this faradaic process exhibited reversibility for smaller voltages, but then became irreversible above 3.2 V. For some electrolytes, like $TEABF_4$ in acetonitrile, one may also observe a small bump in the voltage-time curve similar to that seen in Fig. 4 a) above 3.2 V. Increasing the temperature as in Fig. 4 b) appears to smoothen out some of the irregularities, although the deviation from Eq. (15) can still be observed at higher voltages. These considerations do suggest that redox-kinetics may play an important role

determining V_0, and that this redox-kinetics is related to the electrolyte voltage window. The obtained V_0 from fitting Eq. (15) to the experimental data may provide insight into the range and accuracy over which this equation is valid.

Since Eq. (15) can be fitted to the data, it is clear that one can also use these data to determine C_0 and τ from Eq. (22). If Eq. (22) is used, the voltage saturates at V_0 due to a diverging capacitance, which is unphysical. However, from an operational industrial view the equivalent circuits in Fig. 2 a) and d) are of similar value. In principle, any suitable nonlinear function may be fitted to the experimental galvanostatic charging/discharging curves, as demonstrated in ref. [22]. However, these functions may not easily be interpreted in terms of physical processes, and the energy or charge storage cannot be determined with confidence without considering dissipative processes. From an instrumental point of view it is only the efficiency of the numerical algorithm implementing Eq. (22) and the corresponding equivalent circuit in Fig. 2 d) determines whether it is more useful than the electrical equivalent circuit in Fig. 2 a) in industrial operations. However, if one is interested in the detailed charging mechanisms, there is from a fundamental point of view a large difference between the two equivalent circuits, and the question is now how one should interpret a voltage-dependent capacitance C(V). This question becomes even more important since it is known that some researchers have suggested to interpret the nonlinearity of galvanostatic charging curves entirely in terms of a voltage-dependent capacitance [65]. The theory leading to Eq. (11) is derived assuming an averaging over many local processes, and does not explicitly account for any voltage-dependence. Whether there is any voltage dependence of the capacitance can only be assessed by analyzing experimental data using a method that also accounts for the dissipative processes, as detailed in Section 2.

In ref. [66] it was argued that any change dQ in the electric charge depends on the electrode potential E, and that one should utilize a pseudocapacitance defined as $C = dQ/dE$. For small values of the voltage, Eq. (22) becomes a linear function of voltage, as often assumed when modelling supercapacitors [56,57]. Such a linear function of voltage was reported in ref. [66] even at higher voltages. Supporting voltage-dependence of a capacitor one may think is the observation of voltage dependence that is often quoted for planar electrical double layers [36,39]. This formula is sometimes used as a starting point to explain the capacitance of with porous carbon electrodes used in supercapacitors [19]. However, it should also be noted that a porous carbon electrode consists of a series of irregular surfaces which support both dissipative and charge storage processes, which during charging may give rise to an irregular electrical double layer taking on a range of different thicknesses and voltage-dependencies that deviates from that of the planar situation. While theories based on the Poisson-Boltzmann equation have been developed to determine capacitance of rough electrical double layers [67], these models are based on an equilibrium-situation and are usually without proper loss mechanisms. A conceptual problem is therefore to separate charge transfer associated with losses and charge storage in the electrical double layer, without tangling these two quantities in a manner that makes it challenging to use the concept capacitance at all. Without proper separation of these mechanisms, one may obtain capacitances that differ depending on the technique used, as detailed in ref. [26]. Based on these arguments, the equivalent circuit in Fig. 2 a) is believed to provide a better representation of the supercapacitor than that of Fig. 2 d).

It might be argued that molecular dynamics [68] or ab-initio simulations [69] of the charging process would provide an even better approach to analyzing the data. Clearly, these processes can take into account the detailed structure consisting of a large number of charge-storing (capacitive) and dissipative (resistive) sites in the porous carbon, and not only lumped into a simplified equivalent circuit as in Fig. 2, thus allowing better insight into the contribution of individual pores. However, such models are often very time-consuming and not straightforward to adapt. Moreover, they rely on a number of assumptions related to molecular interactions, configuration and boundary conditions that currently are very difficult, if not impossible, to verify experimentally. The fact is that to date no such small-scale theory has been able to reproduce the voltage versus time charging curves of macroscopic supercapacitors, accounting for both charging time scale and environment-dependent nonlinearities.

Based on the arguments above, the theory of Section 2.1 leading to Eq. (15) and the equivalent circuit in Fig. 1 a) will be used as the main formula fitted to the experimental data. It has been shown by the author in previous publications that also cyclic voltammetry and impedance spectroscopy can be interpreted in terms of the equivalent circuit of Fig. 2 a) when applied to commercial supercapacitors similar to those listed in Section 3 [26,54]. However, as detailed in ref. [26] it is very important to point out that cyclic voltammetry and impedance spectroscopy work under different current conditions than galvanostatic charging, and these former techniques are therefore not always suitable for validating equivalent circuit models to be used under different constant currents. The best way to check the validity of the equivalent circuit is to check the consistency of the data extracted from galvanostatic charging under different circumstances, as will be detailed in this work.

5. Impact of charging current

The supercapacitors were first emptied for charge as described in Section 3, and then charged at a constant current I_0 while the voltage across the two terminals was measured. To stay well within the electrochemical stability window, the supercapacitors were charged up to 2.1 V. All the measurements reported in this section were done at room temperature, $T = 293$ K.

Examples of a voltage-time curve are shown in Fig. 5 for a supercapacitor of manufacturer-given capacitance of 1000 F (SC5). The red curve is the experimental data for $I_0 = 30$A, and the corresponding dashed line is a fit of Eq. (15) with $C_1 = 782$ F, $R_1 = 0.12\ \Omega$, $\tau = 97$ s and $R_s = 8.1$ mΩ. The green curve is the experimental data for $I_0 = 1$ A, and the corresponding dashed line a fit of Eq. (15) with $C_1 = 832$ F, $R_1 = 4.4\ \Omega$, $\tau = 3685$ s and $R_s = 5.0$ mΩ. The orange curve corresponds to $I_0 = 0.3$A, and the dashed line a fit of Eq. (15) with $C_1 = 770$ F, $R_1 = 13.6\ \Omega$, $\tau = 10{,}475$ s and $R_s = 4.6$ mΩ.

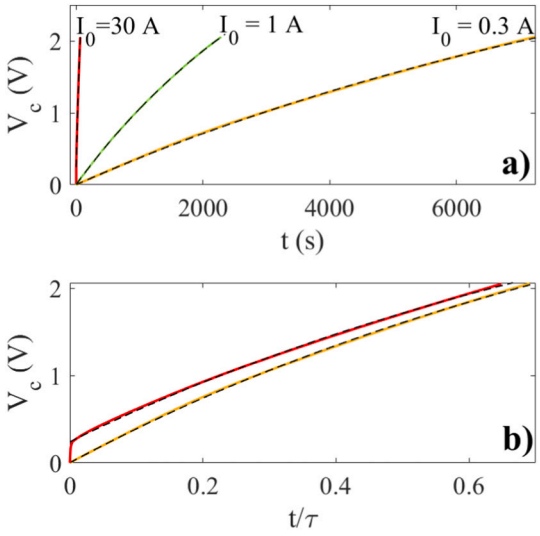

Fig. 5. Charging of the SC5 supercapacitor for $I_0 = 0.3$ A (orange), $I_0 = 1$ A (green) and $I_0 = 30$ A (red). The dashed curves are fits of Eq. (15) to the experimental data. In b) the voltage is shown as function of the reduced time t/τ to better show the difference between the low and high-current curve forms. (For interpretation of the references to colour in this figure legend, the reader is referred to the web version of this article.)

In Fig. 5 b) the same voltage-time curves as in Fig. 5 a) are shown for $I_0 = 0.3$ A (orange) and $I_0 = 30$ A (red), but now as a function of the reduced time t/τ to better show the difference between the low and high-current curve forms. From the fitted parameters for C_1 at different currents, it is observed that the capacitance varies between 770 F and 832 F, which are slightly below the nominal value of 1000 F stated by the manufacturer. Perhaps more peculiar, it was observed that the parallel resistance R_1 decreased from 13.6 Ω at $I_0 = 0.3$ A to 0.12 Ω at $I_0 = 30$ A. In fact, most of the change in curve shape seen in Fig. 5 b) is due to the change in R_1.

Galvanostatic charging curves for different currents were recorded for all the supercapacitors listed in Section 3, and the corresponding fitted parameters V_0, R_1, C_1 and τ are displayed in Fig. 6. It is seen in Fig. 6 a) that V_0 varies between 3 V and 8 V, with an average value about 5 V. The uncertainty in this fitted parameter is rather large (up to 30 %). Some of these variations could be partially attributed to the fact that the maximum charging voltage was kept at 2.1 V such that one did utilize the entire nonlinear range as in Fig. 3. However, it was found that charging to voltages close to or above the manufacturer-given voltage stability window, the charging curves failed to exhibit sufficient repeatability when repeating for different currents or upon using cyclic voltammetry as in ref. [26]. Thus, there were practical reasons for not extending the voltage charging range.

On a more fundamental level, it should also be noted that the extracted V_0 is based on reversible kinetics described by Eq. (15), while the actual maximum voltage is determined by irreversible kinetics as indicated for the voltages above 3.2 V in Fig. 4. Nonetheless, the data in Fig. 6 a) does suggest that there are no systematic variations of V_0 with current, which is in agreement with the theory proposed in Section 2. According to the theory of Section 2, V_0 is determined by the applied current and resistance R_1 according to $V_0 = R_1 I_0$. Moreover, R_1 is inversely proportional to the current and determined by the parallel resistance, which could be due to redox kinetics or ion insertion.

The extracted time constants in Fig. 6 b) show that this parameter is decreasing with increasing current for all supercapacitors investigated. Interestingly, the extracted values for R_1 show an inversely proportionality with applied current, as shown in Fig. 6 c). The dashed line in Fig. 6 c) is given by $R_1 = V_0/I_0$, where $V_0 = 5$ V. This is consistent with the theory developed in Section 2 for the surface reorganization resistance R_{ro} (Eq. (8)) and the charge transfer resistance R_{ct} (Eq. (10)), which both are inversely proportional to the applied current I_0. Thus, in principle both mechanisms may be responsible for the behavior seen in Fig. 6 c).

If one assumes that $C_1 = \varepsilon_0\varepsilon_r A/d \approx 1000$ F with $d \approx 10^{-9}$ m, the area is $A \approx 10^4$ m^2. If one also assumes that the parallel resistance is 0.1 Ω and entirely governed by surface area expansion, then one has that the largest possible change in area is $dA/dt = d/(\varepsilon_r\varepsilon_0 R_{ro}) \approx 10^2$ m^2/s. According to Fig. 6 b), the time constant is about $\tau \approx 10^2$ s for this value of the parallel resistance. The largest currents therefore cannot govern the intercalation and ion insertion since that would lead to a large change in area and therefore most likely also a change in capacitance with time, as is not seen in the observed data. However, no such restrictions exist on small currents wherein a larger R_1 and therefore smaller dA/dt would lead to insignificant changes in area and C_1.

If one assumes that the charge transfer through Eq. (10) is entirely responsible for the current-dependent parallel resistance R_1, one obtains $k_r \approx k_B T/eV_0 \approx 5\bullet10^{-3}$ at room temperature with $k_B T/e = 0.025$ V, which means that the redox current $I_{rA} = k_r I_0$ is about 0.5 % of the of the total current I_0. Clearly, this is a rather inaccurate estimate since Eq. (10) assumes low voltages. Additional information obtained with other measurement techniques is needed to investigate how reasonable this number is.

As shown in Fig. 6 d), we find that the capacitance C_1 of each investigated supercapacitor is constant to within the combined measurement and data fitting uncertainties. These two observations, namely that the parallel resistance is inversely proportional to current, and the capacitance is independent of current, are two of the major findings in this work. Given that the investigated data are extracted for several different supercapacitor taken over currents varying by more than four orders of magnitude place strong confidence in the validity of the data.

The series resistance R_s was also extracted as a function of current I_0, and the results are for clarity shown for each supercapacitor in Fig. 7. It

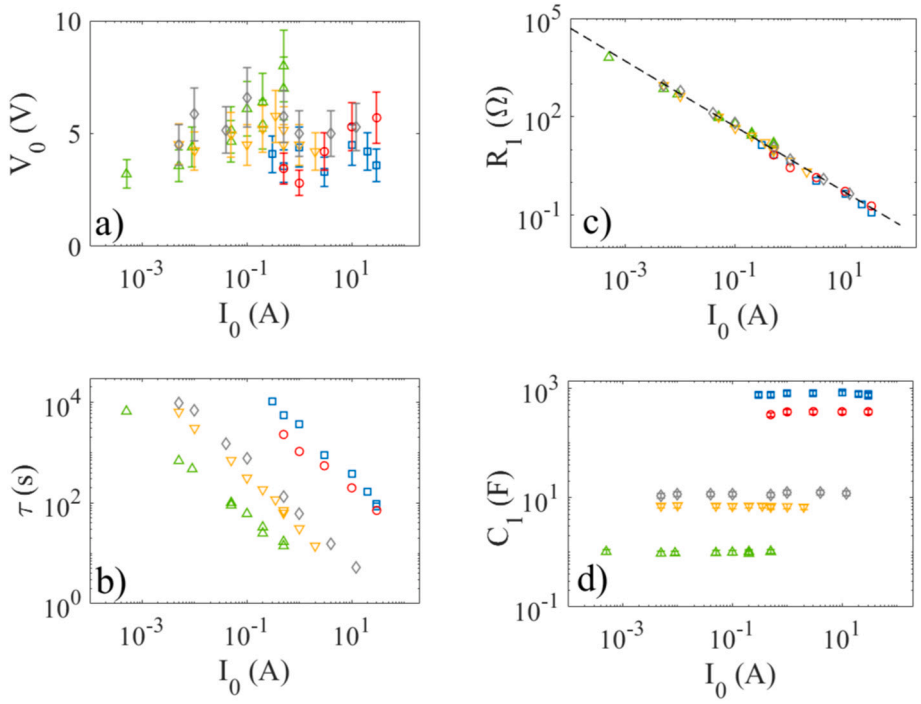

Fig. 6. Fitting parameters V_0 (a), τ (b), R_1 (c) and C_1 (d) obtained using Eq. (15) on experimental voltage-time charging curves. The green upwards triangles correspond to SC1, the grey diamonds to SC2, the orange downwards triangles to SC3, the red circles to SC4 and the blue boxes to SC5. The dashed line in c) is $R_1 = V_0/I_0$, where $V_0 = 5$ V. (For interpretation of the references to colour in this figure legend, the reader is referred to the web version of this article.)

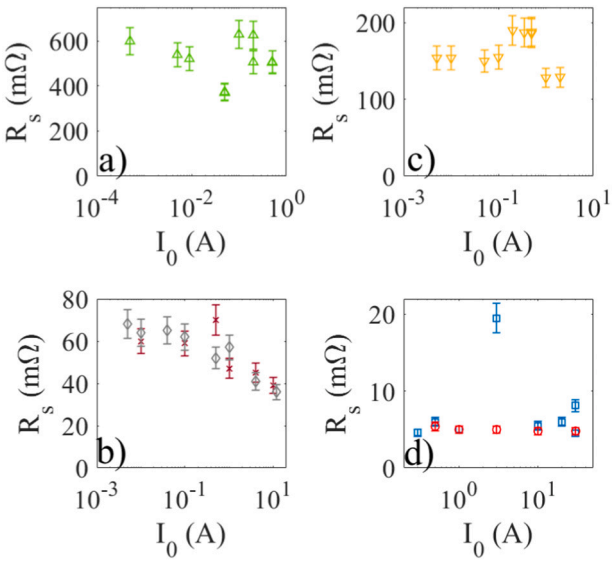

Fig. 7. The serial resistance as a function of current. V_0 (a), t (b), R_1 (c) and C_1 (d) obtained using Eq. (15) on experimental voltage-time charging curves. The green upwards triangles correspond to SC1 (a), the grey diamonds to SC2 (b), the brown crosses to another supercapacitor of the same type as SC2, the orange downwards triangles to SC3 (c), the red circles to SC4 (d) and the blue boxes to SC5 (d). (For interpretation of the references to colour in this figure legend, the reader is referred to the web version of this article.)

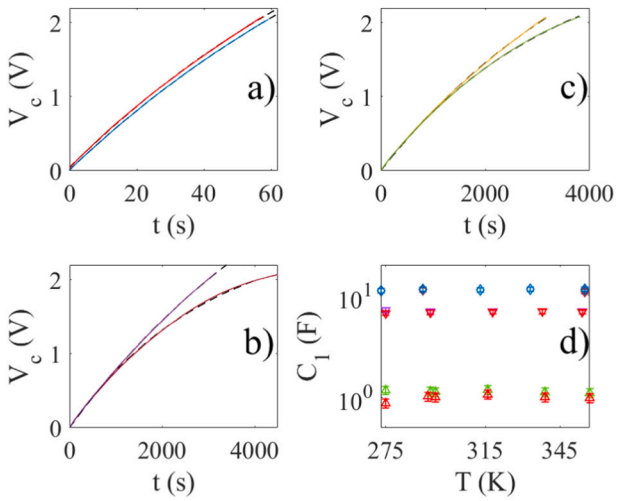

Fig. 8. In a) supercapacitor SC2 is charged at $I_0 = 0.5$ A at T = 273 K (red line) and T = 355 K (blue line). In b), supercapacitor SC1 is charged at $I_0 = 0.001$ A at 275 K (violet line) and 357 K (brown line). In c), supercapacitor SC2 is charged at $I_0 = 0.01$ A at T = 273 K (orange line) and T = 355 K (green line). In d), the extracted capacitance C_1 versus temperature is shown for SC2 charged at $I_0 = 0.5$ A (blue diamond), SC2 charged at $I_0 = 0.01$ A (brown diamond), SC3 charged at $I_0 = 0.5$ A (red downwards triangles), SC3 charged at $I_0 = 0.01$ A (violet downwards triangles), SC1 charged at $I_0 = 0.5$ A (red upwards triangles) and SC1 charged at $I_0 = 0.001$ A (green upwards triangles). (For interpretation of the references to colour in this figure legend, the reader is referred to the web version of this article.)

was found that the series resistance mostly remained independent of current, or at least did not show any systematic variations, with a few exceptions. One exception was observed for SC2 in Fig. 7 b), where the series resistance appears to decrease with current. The result was found to vary a little bit from device to device of the same type of capacitor, see for example the brown crosses in Fig. 7 b) which represent another supercapacitor of nominal 10 F from the same manufacturer. It is currently not known why the series resistance decreases with current, although it could be related to electrical paths that open up as the current increases. Another clear deviation from expectations is the outlier seen in Fig. 7 d) for SC5. Upon repeating the experiment several times, the same behavior was found, but currently no explanation exists for such a behavior.

A decreasing equivalent series resistance with current was also observed in ref. [70]. In ref. [70] this decrease was attributed to a shift in the ionic storage location from smaller pores at low currents to larger pores at higher currents. In the current work, the equivalent series resistance is interpreted as due to charge movement through bulk, at metallic interfaces, and past porous structures, and not a part of charge storage. We find that the equivalent series is independent of current in most cases, with some exceptions, which suggests that the storage location within pores is not responsible for the behavior of R_s with current.

6. Impact of temperature

Using the temperature-controlled measurement setup described in Section 3, the voltage-time curve was measured for the three supercapacitors SC1 (nominally 1 F), SC2 (nominally 10 F) and SC3 (nominally 10 F).

Fig. 8 a) shows the voltage versus time over a supercapacitor of nominal capacitance 10 F (SC2) when the temperature is T = 273 K (red line) and T = 355 K (blue line) during galvanostatic charging with $I_0 = 0.5$ A. In Fig. 8 c), the same supercapacitor is charged at $I_0 = 0.01$ A at T = 273 K (orange line) and T = 355 K (green line). The curves in Fig. 8 a) and c) clearly indicate that both temperature and current influence the charging of the supercapacitor. Further evidence of this is shown in Fig. 8 b) for a supercapacitor of nominal capacitance 1 F (SC1) charged with $I_0 = 0.001$ A at T = 275 K (violet line) and T = 357 K (brown line). All the dashed lines in Fig. 8 a) - c) are fits of Eq. (15) to the experimental data, and the excellent fits suggest that this model provides a good starting point for further analysis.

The extracted capacitances are shown in Fig. 8 d) to remain nearly independent of temperature and also independent of the current to within the accuracy which the measurement and extraction procedure can be done.

The parallel resistance R_1 was extracted from the measurements, and is reported in Fig. 9. In Fig. 9 a), the values of R_1 for SC2 (blue diamonds) and SC3 (red upwards triangles) are reported when charged at $I_0 = 0.01$ A, whereas Fig. 9 b) reports for SC2 (blue diamonds) and SC3 (red upwards triangles) for $I_0 = 0.5$ A. It is seen that the parallel resistance R_1 depends strongly on current as reported in Fig. 6, but much less on temperature for the capacitors SC2 and SC3. While the larger current $I_0 = 0.5$ A in Fig. 9 b) appears to gives rise to no systematic or easily detectable change in parallel resistance, the smaller current in Fig. 9 a) does appear to suggest a small decrease in R_1 with temperature.

Fig. 9 b) shows the parallel resistance R_1 of SC1 charged at $I_0 = 0.5$ A (green upwards triangles), while Fig. 9 c) shows R_1 for SC1 when charged at $I_0 = 0.001$ A. Here it is seen that the large current ($I_0 = 0.5$ A) does not give rise to a clear and systematic temperature-dependent parallel resistance. One clear deviation in Fig. 9 b) is the outlier at 315 K for SC1, but its origin is not known. In Fig. 9 c), there is a clear and systematic decrease in parallel resistance with temperature. The natural logarithm of R_1 versus the inverse of the temperature is plotted in Fig. 9 d). By fitting the linear function $\ln(R_1) = 5.95 + 700/T$ to the data, one obtains the dashed line in Fig. 9 d). This function can also be written as $R_1 = 384\exp(700/T)$, which when interpreted using Eq. (8) results in an energy barrier E = 0.06 eV for area rearrangement during galvanostatic charging. For the data in Fig. 9 a) and b) the corresponding energy barrier is much closer to zero, if the energy barrier proposed in Eq. (8) is assumed to govern behavior. It can also be concluded that Eq. (10) for the charge transfer resistance R_{ct} cannot explain the data, since they do not exhibit an increasing parallel resistance with temperature.

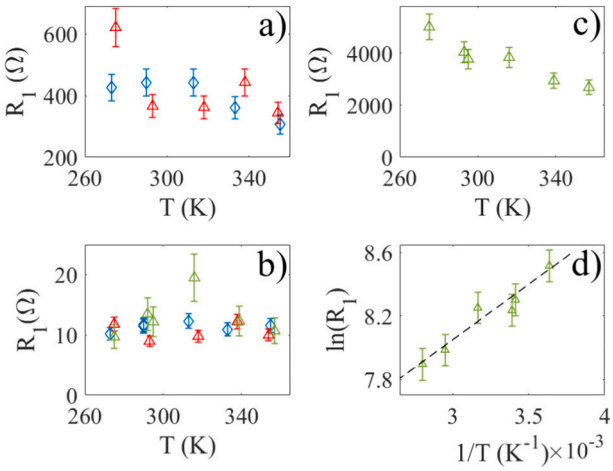

Fig. 9. In a) the resistance R_1 is shown versus temperature for SC2 (blue diamond) and SC3 (red downwards triangles), both charged with a current 0.01A. In b), R_1 is shown versus temperature for SC1 (blue diamond), SC3 (red upwards triangles) and SC1 (green upwards triangles) charged with a current 0.5 A. In c), the green triangles show R_1 for SC1 versus temperature when charged with 0.001 A, whereas in d) the $\ln(R_1)$ is displayed versus the inverse temperature. The dashed line in d) is 5.95 + 700/T. (For interpretation of the references to colour in this figure legend, the reader is referred to the web version of this article.)

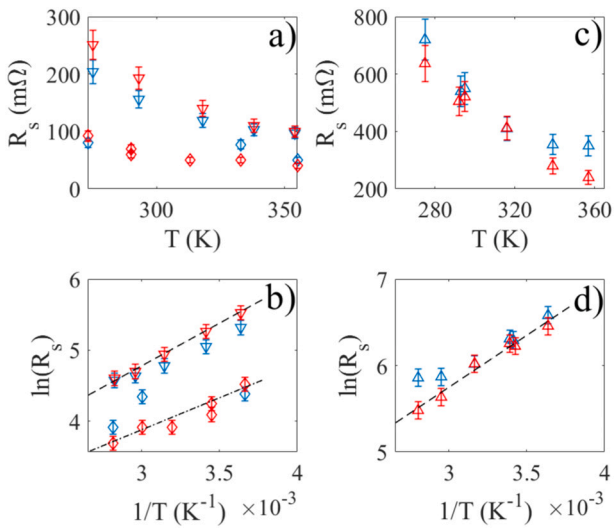

Fig. 10. In a) the serial resistance is plotted versus temperature for SC2 at 0.01 A (blue diamonds) or 0.5 A (red diamonds), and SC3 for 0.01 A (blue downward triangles) and 0.5 A (red downward triangles). In b), the function $\ln(R_s)$ is plotted for the same data, where the dashed line is fit of the function 1.18 + 1200/T and the dash-dotted line is the function 1.18 + 900/T. In c) the serial resistance is plotted versus temperature for SC1 at 0.01 A (blue upwards triangles) and 0.5 A (red upwards triangles). In d) the function $\ln(R_s)$ is plotted for the same data, where the dashed line is the function 2.15 + 1200/T. (For interpretation of the references to colour in this figure legend, the reader is referred to the web version of this article.)

The data from Figs. 6 and 9 seem to suggest that a mechanism similar to that leading to Eq. (8), with the parallel resistance exhibiting a current-dependence which is inversely proportional to the charging current, and a temperature-dependence governed by an energy barrier. The observations further suggests that R_1 decreases with temperature only for smaller currents, which might be associated with an energy barrier associated with movement of charge or increasing the area, similar to that used to derive Eq. (8). This small-current energy barrier is slightly smaller than that associated with self-discharging of supercapacitors [71]. This could be related to larger interactions and flow for higher currents, where such weak barriers are suppressed. However, one also notes in Fig. 9 a) that SC2 only exhibits a noticeable decrease in R_1 at higher temperatures, which appears to suggest that the energy barrier only become relevant above a certain temperature. Similar behavior is not seen for SC3, so it is unclear whether this behavior is just unknown systematic uncertainties or a device-specific behavior.

The series resistance R_s was found to exhibit a clear and systematic decrease with temperature, as demonstrated in Fig. 10 a) for SC2 (red diamond) and SC3 (red downward triangle) charged at $I_0 = 0.5$ A. Also shown is the series resistance of SC2 (blue diamond) and SC3 (blue downward triangle) at $I_0 = 0.01$ A. Similar systematic decrease in series resistance with temperature is also seen for SC1 when charged at $I_0 = 0.5$ A (red upward triangles) and $I_0 = 0.01$ A (blue upward triangles) in Fig. 10 c).

The decrease in serial resistance with temperature has also been reported in ref. [40], where polynomial functions were fit to the experimental data. However, it would be more natural to fit the data to an exponential Arrhenius function to investigate whether an energy barrier might be governing the resistance. In Fig. 10 b) and d) data for the $\ln(R_s)$ is displayed versus the inverse temperature. By fitting the linear function $\ln(R_s) = A_1 + B/T$ to the data, corresponding to an energy barrier which must be overcome to exhibit bulk ionic conduction or electrical contact with the metal collector, one obtains the dashed lines. This function can also be written as $R_s = A_2\exp(E_1/k_BT)$ with $A_2 = \exp.(A_1)$ and $E_1 = k_BB$. From the linear fits in Fig. 10 b) one obtains $E_1 = 0.10$ eV (dashed line) for SC2 and $E_1 = 0.08$ eV (dash-dotted line) for SC3. From the linear fit in Fig. 10 d) one obtains $E_1 = 0.10$ eV (dashed line) for SC1. It is therefore clear that if there are any energy barriers governing the serial resistance R_s, they are comparable to the energy barriers for the parallel resistance R_1 for very small currents. This may indicate that comparable fundamental thermal mechanisms are responsible for the bulk ionic conduction as well as the charge transfer at the surface. However, further studies with other techniques are needed to understand this behavior.

7. Comparison with published research

In this section, we will use data from a selected number of studies [59,72–76] to extract values for R_1 and C_1 in order to compare with the data presented in the previous sections and to point towards possible future directions of supercapacitor research. For practical reasons it is here only possible to consider a selection of works which display voltage-time curves that are possible to read clearly. The data was extracted using the MatLab script called grabit.m.

Since the entire voltage-time curve up to saturation are not normally displayed in the papers investigated, some caution must be made. That is, the interpretation given here relies on the claim that the nonlinearity of the voltage-time curve to be caused by a change in both R_1 and C_1 and can be described by Eq. (15). Although many different criteria for fitting Eq. (15) could be used, here an automated fitting algorithm based on MatLab's nlinfit resulting in $R^2 > 0.99$, combined with subsequent inspection by eye are used to determine whether the fit is satisfactory.

Ideally, the galvanostatic charging should be undertaken after careful and slow discharging followed by a pause to ensure that the supercapacitor does not exhibit rebound effects, as described in the experimental Section 3. However, with few exceptions such as ref. [59], this is not done in reported galvanostatic charging curves found in the literature, which means that many of the curves were not obtained under conditions similar to the experimental data reported in this work.

7.1. Impact of charging current

In Fig. 5 b) of ref. [72], porous carbon consisting of graphene and carbon nanotubes was immersed in tetraethylammonium tetrafluoroborate ($TEABF_4$) and propylene carbonate, and voltage-time

curves reported. Extracted data for two such curves with charging current per area 0.3 mA/cm^2 (black circles) and 3.4 mA/cm^2 (black triangles) are shown in Fig. 11 a). The dashed lines are fits of Eq. (15) to the extracted data with $V_0 = 4.6$ V and $\tau = 1175$ s for 0.3 mA/cm^2, and $V_0 = 5.3$ V and $\tau = 136$ s for 3.4 mA/cm^2.

The curve with the steepest incline in Fig. 5 b) of ref. [72] could not be resolved, but values for V_0 and τ were extracted in a similar manner for the other currents, and the corresponding relative values of R_1 and C_1 are plotted in Fig. 11 b) and c). Note that R_{01} and C_{01} are constants denoting the maximum values, and that we are only reporting the relative values R_1/R_{01} and C_1/C_{01} since the trends are of most importance here.

The dashed line in Fig. 11 b) is a fit to the extracted values representing the function $0.32/I_0$. It appears that the function R_1 decreases by an order of magnitude as the current increases, and is inversely proportional to the charging current I_0, in agreement with the findings of Section 5. Moreover, the capacitance C_1 does not change by more than about 20 %.

In ref. [72] it was reported in Fig. 5 d) that the capacitance decreases with charging current, in particular at the higher currents. Since the voltage-time curves for the highest currents were not reported it is not possible to check this here, but with the findings in Fig. 11 one may question whether it is in fact the parallel resistance, and not so much the capacitance that changes strongly with current. This deviation in interpretation of the capacitance is related to the data extraction technique used, as investigated in ref. [26]. If one takes into account the nonlinearity of the voltage-time curve using Eq. (15) or some other suitable model, a better representation of the capacitance may be obtained.

It is often of interest to observe how different nanostructures influence the galvanostatic charging current. In ref. [73] both pristine and unzipped multiwall carbon nanotubes were used. Fig. 12 a) reports the voltage-time data extracted from Fig. 7 in ref. [73] for a current per electrode mass 0.5 A/g, where the blue circles correspond to pristine nanotubes and the red boxes to unzipped nanotubes. The blue dashed line in Fig. 12 a) corresponds to a fit of Eq. (15) to the extracted data with $V_0 = 5.8$ V and $\tau = 54$ s, whereas the red dashed line corresponds to

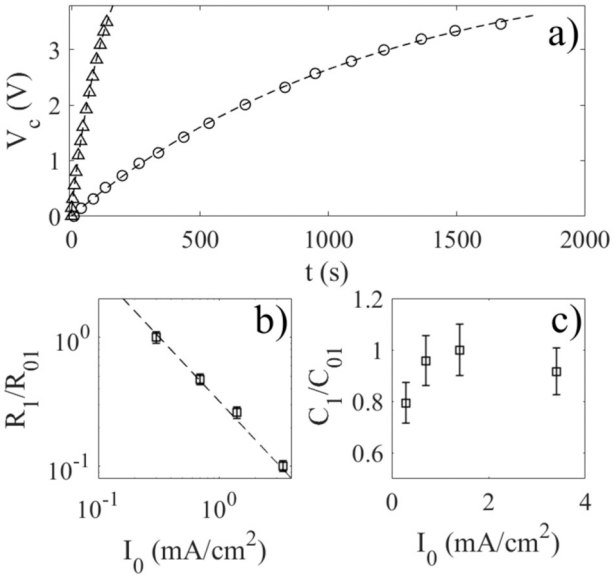

Fig. 11. In a, data points extracted from Fig. 5 b) in ref. [72], corresponding to a charging current per area 0.3 mA/cm^2 (black circles) and 3.4 mA/cm^2 (black triangles), are shown. The dashed lines correspond to fits of Eq. (15) to the extracted data. In b) and c) the extracted relative parallel resistance and capacitance are plotted, respectively. The dashed line in c) is a fit of Eq. (15) to the extracted data. The dashed line in c) is the function $0.32/I_0$.

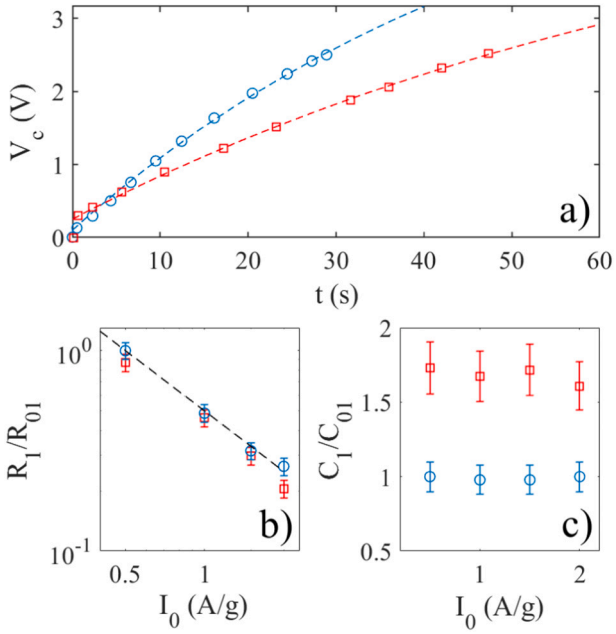

Fig. 12. The circles in a) are data points extracted from Fig. 7 in ref. [73], corresponding to pristine carbon nanotubes (blue circles) and unzipped carbon nanotubes (red squares) samples charged at $I_0 = 0.5$ A/g. The blue dashed line corresponds to a fit of Eq. (15) to the extracted data with $V_0 = 5.8$ V and $\tau = 54$ s, whereas the red dashed line corresponds to fits with $V_0 = 5.1$ V and $\tau = 81$ s. In b), values of R_1/R_{01} for pristine nanotubes (blue circles) and unzipped nanotubes (red squares). The black dashed line in b) is a fit to the extracted data for pristine MWCNT with the function $0.5/I_0$. In c), the relative change in capacitance C_1/C_{01} versus is current is plotted for pristine nanotubes (blue circles) and unzipped nanotubes (red squares). (For interpretation of the references to colour in this figure legend, the reader is referred to the web version of this article.)

fits with $V_0 = 5.1$ V and $\tau = 81$ s. Further extraction of relative values of R_1 and C_1 are plotted in Fig. 12 b) and c). Here R_{01} and C_{01} are constants denoting the maximum values relative to that obtained with pristine multiwalled carbon nanotubes. The dashed line in Fig. 12 b) represents the function $0.5/I_0$, which is a fit to the extracted data for R_1/R_{01}. It suggests that the R_1 is inversely proportional to the current, as was also shown in Fig. 6 c).

The capacitance C_1 is larger for unzipped nanotubes as compared to pristine ones, as seen in Fig. 12 c), which is probably due to the increased area of the former as discussed in ref. [73]. On the other hand, R_1 in Fig. 12 b) does not change much by unzipping the nanotubes may hint to the fact that the redox-reactions or ion insertion does not depend much on the area available. In ref. [73] it is stated that the capacitance decreases with increasing current, see table 1 of ref. [73]. As shown in Fig. 12 c), fitting the data of Fig. 7 in ref. [73] to Eq. (15) results in a capacitance that does not change with current, at least to within the accuracy of the extraction and fitting procedure. Instead, any nonlinearity in the galvanostatic charging curve is associated with the resistance R_1, which is seen to decrease with applied current according to the function $0.5/I_0$.

In addition to the two examples shown here, data from other publications such as ref. [77] have also been extracted and the estimated values of R_1 found to be in good agreement with the inverse current rule proposed in this work. Currently it is not possible to distinguish the exact working mechanism of most of the data reported in the literature based on such plots of parallel resistance versus current alone, since several mechanisms such as surface reorganization (Eq. (8)) or redox-reactions (Eq. (10)) might give rise to an inverse proportionality between R_1 and I_0.

7.2. Impact of temperature

The influence of temperature on the serial resistance R_s is well documented in Fig. 10 and in the literature [40], and will not be further investigated here. However, the temperature dependence of R_1 obtained from galvanostatic charging measurements has never before been reported in the literature, and it is therefore of interest to extract such data and compare it with the theory of Section 2, as well as the data based on experiments and presented in Fig. 9.

Fig. 13 a) and c) show extracted data points from Fig. 9 in ref. [73], corresponding to pristine carbon nanotubes (blue circles) and unzipped carbon nanotubes (red squares) samples charged at $I_0 = 0.5$ A/g at temperature T = 300 K (a) and T = 373 K (c). Eq. (15) is fitted to the experimental data, and the blue dashed line in Fig. 13 a) has $V_0 = 4.7$ V and $\tau = 72$ s and the red dashed line $V_0 = 4.5$ V and $\tau = 35$ s. Similarly, the blue dashed line in Fig. 13 c) has $V_0 = 4.3$ V and $\tau = 40$ s, and the red dashed line $V_0 = 4.3$ V and $\tau = 115$ s. In all these cases it is seen that the voltage V_0 remains relatively unchanged to within 10 %, whereas the time constant τ changes by a factor of more than three. From the fits of Eq. (15), one can extract data for the relative parallel resistance R_1/R_{01} and capacitance C_1/C_{01}. Here R_{01} and C_{01} are the maximum resistance and capacitance, respectively, extracted for the pristine nanotube from data such as those in Fig. 9 in ref. [73].

The data in Fig. 13 b) suggests that the parallel resistance does not change very much with temperature, to within extraction uncertainty, both for the pristine and unzipped nanotubes. This is in agreement with the observations for the commercial supercapacitors, but it might be possible that a smaller current than the 0.5 A/g used in ref. [73] could result in a temperature-dependency. The capacitance C_1 remains constant and independent of temperature for pristine nanotubes, but increases with temperature for unzipped carbon nanotubes, as also noted in ref. [73]. This may indicate that the available area increases as the unzipped carbon nanotube is heated, for example due to gradual opening of pores which then become more accessible to ions. The sudden increase in C_1 above 300 K in Fig. 13 d) is accompanied by a sudden increase in R_1 in Fig. 13 b), which could be due to altered redox-activity on the surface leading to a larger R_1.

The method presented above, using Eq. (15) to extract data for R_1 and C_1, can also be applied on other published research works. In ref. [74], a mixture of 1.4 M Li_2SO_4 and ethylene glycol was combined with

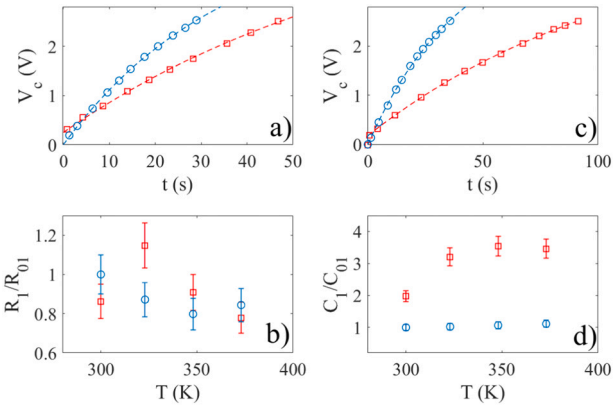

Fig. 13. The data points in a) and b) are data points extracted from Fig. 9 in ref. [73], corresponding to pristine nanotubes (blue circles) and unzipped nanotubes (red squares) samples charged at $I_0 = 0.5$ A/g at temperature T = 300 K (a) and T = 373 K (c). The blue and red dashed lines in corresponds to fits of Eq. (15) to the extracted data. The corresponding extracted data for the relative parallel resistance and capacitance are shown in b) and d), respectively. (For interpretation of the references to colour in this figure legend, the reader is referred to the web version of this article.)

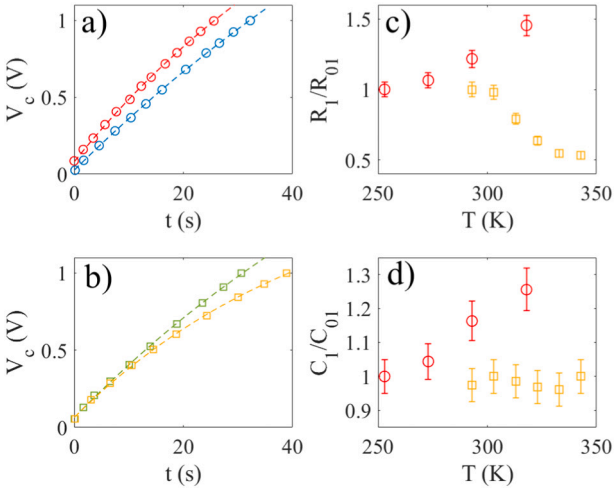

Fig. 14. The circles in a) are data points extracted from Fig. 3 in ref. [74], corresponding to T = 253 K (blue circles) and T = 318 K (red circles). The boxes in b) are data points extracted from Fig. 11 in ref. [75], corresponding to T = 293 K (green) and T = 343 K (orange). The dashed lines in a) and b) are fits to the extracted experimental data using Eq. (15). (For interpretation of the references to colour in this figure legend, the reader is referred to the web version of this article.)

graphene and carbon nanofiber as the electrolyte/electrode combination. Fig. 14 a) shows examples of extracted data points from Fig. 3 a) in Ref. [74], and the dashed lines are fits to Eq. (15). The relative parallel resistance R_1/R_{01} and capacitance C_1/C_{01} are displayed as circles in Fig. 14 c) and d), respectively. The data indicate that both the parallel resistance and capacitance increase with temperature. According to Fig. 3 a) of ref. [74], the serial resistance R_s decreases with temperature, in agreement with data for commercial supercapacitors such as those from Fig. 10.

The increase in capacitance with temperature in Fig. 14 d) may suggest that the area available for charge storage increases with temperature due to an increased access for ions. However, according to Fig. 14 c), it is also seen that the increase in capacitance is accompanied with a monotonous increase in parallel resistance as the temperature increases. This may therefore suggest that $dA/dt < 0$ if Eq. (8) is valid, which may appear to contradict Fig. 14 d) which seems to require that $dA/dt > 0$ for the capacitance to increase. This simplified argument requires that the capacitance is proportional to A and the surface reorganization factor R_{ro} as inversely proportional to dA/dt. In some situations, however, it is not unreasonable to expect that an increase in charge storage area is related not to the total area, but rather the distribution of pore sizes that accept ions for storage in the electrical double layer. Thus, it is possible for the capacitance C_1 to increase while the area decreases, thus leading to an increase in C_1 and R_1 simultaneously. Another possible explanation is an increase in surface active species and therefore redox-activity, leading to an increased R_1 with a simultaneous increase in C_1. The investigations presented here show that further studies are needed to extract the origin of the temperature-behavior.

Behavior consistent with that of Figs. 8 and 9 can also be found in the literature. In ref. [75], 3 M KOH was used as an electrolyte with porous surfaces made of carbonized bamboo. The boxes in Fig. 14 b) are data points extracted from Fig. 11 in ref. [75], corresponding to T = 293 K (green) and T = 343 K (orange), where the dashed lines are fits using Eq. (15). The relative parallel resistance R_1/R_{01} and capacitance C_1/C_{01} are displayed as boxes in Fig. 14 c) and d), respectively. It is seen that the capacitance remains almost constant while the parallel resistance decreases with temperature. This is consistent with the findings of Fig. 9 c), and suggest an energy barrier as detailed in Section 6. It should be noted that in ref. [75] it was claimed that the capacitance increased with temperature, a result which is most likely due to the use of some sort of

averaging over the slopes in the charging/discharging curves. As was pointed out in Section 2, taking into account nonlinearities is required, and this leads to the corrected relative capacitance in Fig. 14 d).

7.3. Impact of aging

Other factors influencing the performance of supercapacitors can also be investigated using nonlinear galvanostatic charging curves. While it is not rare for supercapacitors to last more than a million cycles, aging still remains an important issue for these energy storage devices. A comprehensive analysis of different aging mechanisms and supercapacitor service life was reported in Ref. [66]. Impedance spectroscopy has been used to extract circuit parameters [78] or a distribution of relaxation times [79] as a function of aging time. The capacitance can be used to determine the state of health of supercapacitors [80]. Here we point out that also the nonlinearities of the galvanostatic charging curve should be accounted for in order to extract a value for the capacitance.

In ref. [59] a commercial supercapacitor (BCAP0350 from Maxwell Technologies) was placed at constant temperature 65 °C and 2.9 V for a given time interval to age the supercapacitor, and then discharged and charged at constant current $I_0 = 10$ A. The resistance R_s can be read directly from Figs. 3 b) and 5 in ref. [59], and is seen to increase monotonously with aging time. In Fig. 15 a), data points are extracted from Fig. 3 a) in ref. [59] for initial charging (circles) and after 1751 h of aging (squares). The dashed lines in Fig. 15 a) show fits of Eq. (15) to the experimental data. The fit to the non-aged experimental data is with $C_1 = 296$ F, $R_1 = 0.69$ Ω, $V_0 = 6.9$ V, $R_s = 0.0027$ Ω and $\tau = 203$ s. The fit to the experimental data for supercapacitors aged for 1751 h could be obtained used $C_1 = 208$ F, $R_1 = 0.59$ Ω, $V_0 = 5.9$ V, $R_s = 0.0059$ Ω and $\tau = 122$ s. Similar fits were made for all the voltage-time curves reported in Fig. 3a) of ref. [59], and the resulting values for R_1 and C_1 are shown in Fig. 15 b) and c), respectively.

The data in Fig. 15 demonstrate that the capacitance C_1 clearly decreases with aging as also discussed in ref. [59]. However, from Fig. 15 b) one can also extract the new information that the parallel resistance R_1 remains relatively unchanged to within the uncertainty of the data extraction procedure. The data may suggest that since R_1 remains relatively unchanged, the faradaic currents do not increase with aging. Instead, it is possible that a blocking layer forms which contribute to reduce the capacitance while not influencing the parallel resistance. If this is the case, the increase in serial resistance R_1 with aging is then related to degrading contacts with the metal current collectors or the bulk of the electrolytes, and not the porous carbon surfaces. Blocking layers are also known to reduce self-discharge, and should be further investigated [81–83].

In ref. [76], the influence of moisture and cycle number on supercapacitor performance was investigated. Three types of samples, which initially contained water vapor were investigated. Samples denoted E-6 and E-12 were dried at 100 °C in vacuum for 6 h and 12 h, respectively, and were reported to contain 1.5 mg and 1.0 mg water per gram carbon. The sample denoted E-s was dried for 24 h at 200 °C, and contained only 0.6 mg water per gram carbon.

Fig. 16 a), shows data points extracted from Fig. 4 in Ref. [75]. In Fig. 16 a), the red circles correspond to the initial cycle, whereas the blue circles are data from the 30th cycle for sample E-s from Fig. 4 a) in ref. [76]. The dashed red and blue lines are fits of Eq. (15) to the extracted data using $V_0 = 4.5$ V (red dashed line), $\tau = 487$ s (red dashed line), $V_0 = 3.5$ V (blue dashed line) and $\tau = 310$ s (blue dashed line). In Fig. 16 b), the orange squares correspond to the initial cycle, whereas the green squares are data from the 30th cycle for sample E-12 from Fig. 4 b) in ref. [76]. The dashed orange and green lines are fits of Eq. (15) to the extracted data using $V_0 = 4.0$ V (orange dashed line), $\tau = 411$ s (orange dashed line), $V_0 = 2.1$ V (green dashed line) and $\tau = 103$ s (green dashed line).

In Fig. 16 c) and d), the blue circles correspond to the relative resistance and capacitance of sample E-s, the black triangles to sample E-6, and the green boxes to sample E-12. The resistance and capacitance are normalized against the maximum value for sample E-6, which occurred when the cycle number is small. The capacitance reported in Fig. 16 d) shows a similar decrease with cycle number as that reported in Fig. 5 a) in ref. [76]. In ref. [76] this decrease in capacitance was

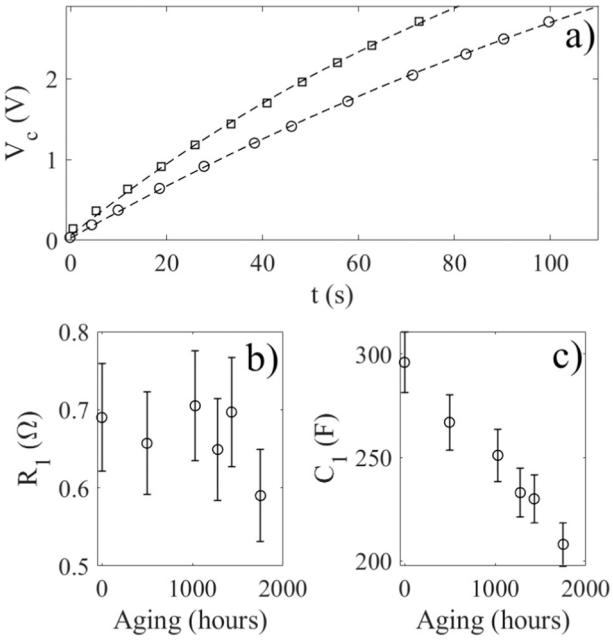

Fig. 15. In a), data points are extracted from Fig. 3a) in ref. [59] for initial charging (circles) and after 1751 h of aging (squares). The charging current is 10 A. The dashed lines show a fit of Eq. (15) to the experimental data. In b) and c), the parallel resistance R_1 and the capacitance C_1 have been extracted as a function of aging, respectively.

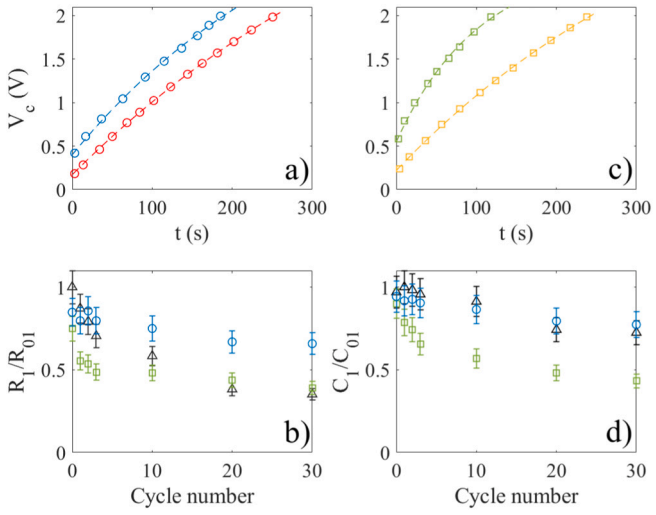

Fig. 16. In a), data points are extracted from Fig. 4 a) in Ref. [76], where the red circles correspond to the initial cycle and the blue circles are data from the 30th cycle for sample E-s. The dashed red and blue lines are fits of Eq. (15) to the extracted data using. In c) extracted data from Fig. 4 b) in Ref. [76] are plotted, the orange squares correspond to the initial cycle, whereas the green squares are data from the 30th cycle for sample E-12. The dashed lines in a) and c) are fits of Eq. (15) to the experimental data. In b) and d), the relative parallel resistance R_1/R_{01} and capacitance C_1/C_{01} are plotted for samples Es (blue circles), E-12 (green squares) and E-6 (black boxes). (For interpretation of the references to colour in this figure legend, the reader is referred to the web version of this article.)

explained to be due to residual insoluble products or other blocking structures, which could be compared to the situation of Fig. 15 c). Fig. 16 c) appears to suggest that the parallel resistance R_1 decreases with cycle number and water content of the sample, which might be explained by increased redox-activity or gradual increase of surface access for water-dissolved ions as the cycling proceeds. This latter hypothesis is further supported by the reported increase in serial resistance R_s as reported in Fig. 5 b) of ref. [76]. Contradicting this hypothesis and apparently also the values for R_1 extracted in Fig. 16 b) is the statement in ref. [76] that the impedance spectrogram of Fig. 6 suggests a larger 'interfacial resistance' with aging. For several different reasons one should be careful when comparing the resistance R_1 extracted during galvanostatic charging with that qualitatively observed from an impedance spectrogram. First, care must be taken when extracting dissipative and capacitive elements from a complex impedance spectrogram, as one otherwise may end up with noncomparable electrical equivalent circuits. Second, charging with a specific large current is usually favoring a specific or a very limited range of kinetic processes, while in an impedance spectrogram a whole range of frequencies are investigated. Thus, forcing charge back and forth at the same rate many times may result in a gateway of reduced resistance during galvanostatic charging, an effect not seen in impedance spectroscopy where many frequencies are applied in sequence. This is indeed what the extracted data in Fig. 16 b) suggest, if the interpretation of using Eq. (15) to extract R_1 and C_1 is correct. It could also be that such a decrease in resistance is also presented in the supercapacitor analyzed in ref. [59] and Fig. 15 b), but that it is smaller than the uncertainty due to the data extraction procedure. The observation in Fig. 16 b) of a significantly reduced resistance with aging could then be interpreted as due to water.

These findings reported here should also be put in context with the observed self-discharge of supercapacitors, which could occur due to leakage currents in the electrolyte or electrodes, redox-reactions at the electrode surface or redistribution of charge on the porous electrode surface [84–94]. During self-discharge, the surface chemistry plays an important role [95,96], and aging may influence the self-discharge considerably. In ref. [97], a similar electrical equivalent model as in Fig. 2 a) was proposed to describe self-discharge, exhibiting a current-dependent parallel resistance. Further correlation of the behavior between charging/discharging and self-discharging behavior during aging, and might bring additional insight into the mechanisms for parallel resistance, but this outside the scope of this work.

8. Classification of galvanostatic charging curves

In the previous sections, we have only considered one type of galvanostatic charging curves, which can be described by Eq. (15). Such curves will in the following be denoted type-i curves exhibiting a convex shape. These are perhaps the most often observed curves in the literature [26–28,54,59,62,64–66,72–77]. The origin of the resistance R_1 of type-i curves is either due to charge transfer or surface reorganization resistance, a combination thereof, or due to surface active species, as discussed extensively in the previous sections. However, this type of galvanostatic voltage-time curve is not the only one observed in the literature.

One possible method to classify the galvanostatic charging curves observed in the literature is according to schematics proposed in Fig. 17. Type-ii curves have a concave shape as shown in Fig. 16 b), and are occasionally reported in the literature, see for example Fig. 5 c) of ref. [98–100]. Such curves are often associated with battery-like behavior [30–34]. For an entirely reversible reduction-oxidation reaction, such as seen in rechargeable batteries, the time-dependent concentration obtained by solving the diffusion equation is inserted in the Nernst equation to obtain $V_C = V_1 + (RT / nF)\ln[(\gamma^{1/2} - t^{1/2}) / t^{1/2}]$, where V_1 is a constant, R is the universal gas constant, F is the Faraday constant, n is the number of moles of electrons participating in the charge transfer reaction, and γ is a transition time given by the Sand equation [101].

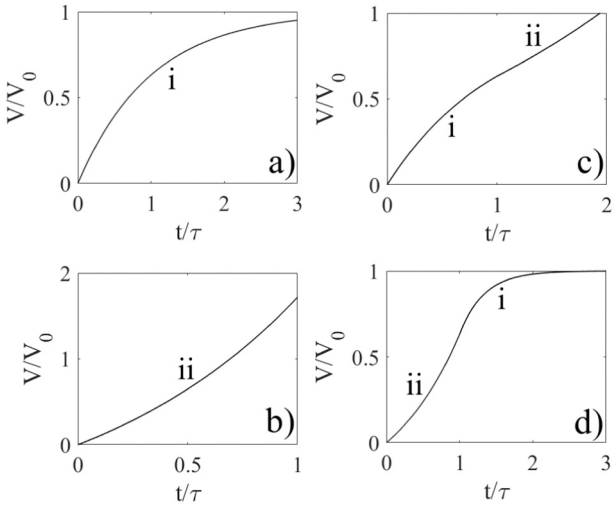

Fig. 17. The different types of galvanostatic charging curves. In a) convex type-I curves are shown, whereas in b) concave type-ii) curves are shown. In b) and d) combinations of type-I and type-ii curves are shown.

This equation is useful to explain the behavior of rechargeable batteries, which rely on reversible charge transfer reactions, wherein a characteristic is that the voltage nearly saturates before it eventually starts to increase significantly as $t \to \gamma$. However, there is no indication of such reversible charge transfer reactions occur in supercapacitors such as those studied here.

However, the occurrence of type-ii curves shown in Fig. 17 b) does not require reversible charge-transfer reactions and may also occur as a result of low electrolyte concentration. For example, initial type-ii behavior was reported in ref. [99] as possibly due to insufficient electrolyte concentration resulting in electrolyte starvation. Electrolyte starvation gives rise to gradual ion depletion from the porous carbon surface. This could be described by a diffusion current $I_d = -eADdn/dx$ in Eq. (1), where D is the diffusion coefficient. If the diffusion is governed by activation by energy barriers, it will exhibit a similar form as in Eq. (7). The minus sign shows that the ions move away from the surface from high to low ion concentration. The diffusion current is therefore negative, and would contribute to the sign of the current in the same manner as a decreasing area rate ($dA/dt < 0$). Following this line of interpretation, one could claim that the apparent parallel resistance R_1 becomes negative such that $R_1C_1 < 0$. Defining $t = |R_1C_1|$ as a constant and solving Eq. (13) gives rise to the following voltage across the supercapacitor:

$$V_c(t) = V_0\left(e^{t/\tau} - 1\right) + R_s I_0. \tag{23}$$

The voltage represented by Eq. (23) gives rise to a convex curve of the type shown in Fig. 17 b). It is obvious that type-ii behavior can only be possible within a limited voltage window, and that the exponential function cannot grow indefinitely, as Eq. (23) only remains valid within the stability window of the electrolyte. That is, one expects that Eq. (23) loses validity when t approaches τ, and that under such conditions the full Eq. (13) must be solved with an unknown time-dependent $\tau(t)$. This is a rather difficult task.

It is also possible to have a combination of different types of behaviors. For example, it is sometimes observed that the voltage-curve is first convex (type-i) before it becomes concave (type-ii), as reported in Fig. 7 in ref. [98], Fig. 7 of ref. [99] or Fig. 5 of ref. [100]. It could be related to a gradual change in properties, for example from faradaic processes to electrolyte depletion. Finally, one may also encounter type-ii followed by type-i processes.

In ref. [99] it was demonstrated that using a sub-optimal electrolyte concentration result in galvanostatic charging curves which first exhibit

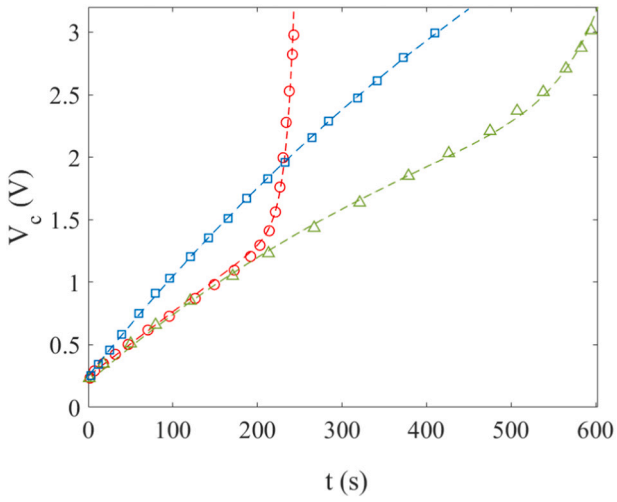

Fig. 18. The blue boxes correspond to 1 M electrolyte, the red circles to 0.2 M and the green triangles 0.08 M. The experimental data are extracted from Figs. 6 a), 7 a) and 8 a) in ref. [99]. The corresponding dashed lines are fits to the experimental data using Eq. (24). The current was 1 A. See text for details. (For interpretation of the references to colour in this figure legend, the reader is referred to the web version of this article.)

type-i and subsequently type-ii behavior. This was in ref. [99] interpreted as 'electrolyte starvation' due to depletion of ions. Here, this is interpreted as the parallel resistance R_1 changes from positive to negative. A transition to negative R_1 does not happen abruptly, and it should be noted that R_1 is time-dependent $R_1(t)$. Since the time-dependence of R_1 is not known, one could extract it from the voltage-time data. Alternatively, one could also make the ad-hoc assumption that the voltage curve is a sum of two time-scales, wherein one with $R_1 > 0$ sets in at $t = 0$ and is represented by the time constant τ, while the other with $R_1 < 0$ sets in when ion depletion becomes important after a time t_1 and is represented by the time constant τ_1. The resulting function can be approximated by

$$V_c(t) = V_0\left(1 - e^{-t/\tau}\right) + V_1\left(e^{(t-t_1)/\tau_1} - 1\right) + R_s I_0. \quad (24)$$

The dashed blue line in Fig. 18 corresponds to a fit of Eq. (24) to the experimental data with $C_1 = 118$ F, $R_1 = 7.0\ \Omega$, $\tau = 823$ s, $R_s = 0.25\ \Omega$, the green dashed line to and $C_1 = 170$ F, $R_1 = 3.5\ \Omega$, $\tau = 590$ s, $R_s = 0.30\ \Omega$, $V_1 = 0.1$ V, $\tau_1 = 50$ s and $t_1 = 500$ s and the red dashed line $C_1 = 194$ F, $R_1 = 66\ \Omega$, $\tau = 1288$ s, $R_s = 0.35\ \Omega$, $V_1 = 0.1$ V, $\tau_1 = 10$ s and $t_1 = 215$ s.

The extracted values for R_1 corresponding to the red dashed line is too large (giving a too large V_0), and it is not possible to justify it as a traditional resistance as defined in Section 2. However, the excellent fits of Eq. (24) to the experimental data extracted from ref. [98] suggest that the approach given here is feasible and worth investigating further also for other experimental data on an empirical basis. It would be of interest to further investigate the relationship between the model of Eq. (11) and the molecular origin of the galvanostatic voltage-time curves given in Fig. 17. However, such studies are outside the scope of the current work.

9. Conclusion

This work investigates the origin and consequences of the nonlinearities of the voltage-time curves measured during galvanostatic charging of supercapacitors. Such voltage-time curves are often used to determine the capacitance of supercapacitors, under the assumption of linearity. However, here it is pointed out that the nonlinearity should be taken into account when analyzing the galvanostatic charging curves, and that the nonlinearity contains additional information that has not been analyzed in a systematic manner in the literature. It is found that the parallel resistance due to either charge transfer or surface reorganization is governing the nonlinearity in commercial supercapacitors based on porous carbon structures in organic electrolyte, and that this resistance decreases inversely with the applied current. The temperature-dependence appears to suggest activation over an energy barrier at lower currents, which becomes unimportant at higher currents.

The findings are compared with experimental data found in the literature. It is demonstrated that the method presented here can be used to analyze aging of supercapacitors, where it is found that the parallel resistance remains either relatively constant or decreases with aging time.

Finally, a classification of nonlinear charging curves is proposed, together with semi-empirical formulas for the voltage which can be used to distinguish different types of behaviors. These may also turn out to be useful when comparing the behavior of supercapacitors based on porous carbon structures with pseudocapacitors utilizing faradaic reactions.

CRediT authorship contribution statement

All the work presented here was performed by Lars Egil Helseth, including development of theory, all experimental work, modelling and writing the manuscript. No particular funding was received to do this work. The author declares no conflict of interests with anyone regarding this work.

Declaration of competing interest

The authors declare that they have no known competing financial interests or personal relationships that could have appeared to influence the work reported in this paper.

Data availability

Data will be made available on request.

References

[1] H.I. Becker, U.S. pat., 2800.616 to General Electric Co, 1957.
[2] B.E. Conway, Electrochemical Supercapacitors, Kluwer Academic, New York, USA, 1999.
[3] D.P. Dubal, Y.P. Wu, R. Holze, Supercapacitors: from the Leyden jar to electric buses, ChemTexts 2 (2016) 13.
[4] S. Satpathy, S. Das, B.K. Bhattacharyya, How and when to use super-capacitors effectively, an integration of review of past and new characterization works on super-capacitors, J. Energy Storage 27 (2020), 101044.
[5] R.L. Spyker, R.M. Nelms, Classical equivalent circuit parameters for a double-layer capacitor, IEEE Trans. Aerosp. Electron. Syst. 36 (2000) 829–836.
[6] J.R. Miller, Engineering electrochemical capacitor applications, J. Power Sources 326 (2016) 726–735.
[7] R.T. Yadlapalli, R.R. Alla, R. Kandipati, A. Kotapati, Super capacitors for energy storage: progress, applications and challenges, J. Energy Storage 49 (2022), 104194.
[8] C.T. Sarr, M.B. Camara, B. Dakyo, Supercapacitors aging assessment in wind/tidal intermittent energies application with variable temperature, J. Energy Storage 46 (2022), 103790.
[9] A. Weddell, G. Merrett, T. Kazmierski, B. Al-Hashimi, Accurate supercapacitor modeling for energy harvesting wireless sensor nodes, IEEE Trans. Circuits Syst, II Exp Briefs 58 (2011) 911–915.
[10] Y. Zhang, H. Yang, Modeling and characterization of supercapacitors for wireless sensor network applications, J. Power Sources 196 (2011) 4128–4135.
[11] H. Yang, Y. Zhang, A study of supercapacitor charge redistribution for applications in environmentally powered wireless sensor nodes, J. Power Sources 273 (2015) 223–236.
[12] S. Pohlmann, Metrics and methods for moving from research to innovation in energy storage, Nature Commun. 13 (2022) 1538.
[13] A. Balducci, Electrolytes for high voltage electrochemical double layer capacitors: a perspective article, J. Power Sources 326 (2016) 534–540.
[14] X. Zhang, X. Wang, L. Jiang, H. Wu, C. Wu, J. Su, Effect of aqueous electrolytes on the electrochemical behaviors of supercapacitors based on hierarchically porous carbon, J. Power Sources 216 (2012) 290–296.
[15] X. Wang, R.S. Chandrabose, S.E. Chun, T. Zhang, B. Evanko, Z. Jian, S. W. Boettcher, G.D. Stucky, X. Ji, High energy density aqueous electrochemical capacitors with a KI-KOH electrolyte, ACS Appl. Mat. & Int. 7 (2015) 19978–19985.

[16] B. Akinwolemiwa, C. Peng, G.Z. Chen, Redox electrolytes in supercapacitors, J. Electrochem. Soc. 162 (2015) A5054–A5059.
[17] P.W. Ruch, D. Cericola, A. Forelske-Schmitz, R. Kotz, A. Wokaun, Aging of electrochemical double layer capacitors with acetonitrile-based electrolyte at elevated voltages, Electrochim. Acta 55 (2010) 4412–4420.
[18] Q. Dou, H.S. Park, Perspective on high-energy carbon-based supercapacitors, Energy Environ. Mater. 3 (2020) 286–305.
[19] H. Shao, Y.C. Wu, Z. Li, P.L. Taberna, P. Simon, Nanoporous carbon for electrochemical capacitive energy storage, Chem. Soc. Rev. 49 (2020) 3005.
[20] C. Lämmel, M. Schneider, M. Weiser, A. Michaelis, Investigations of electrochemical double layer capacitor (EDLC) materials - a comparison of test methods, Mat.-wiss. U. Werkstofftech. 44 (2013) 641–649.
[21] N. Devillers, S. Jemei, M.C. Péra, D. Bienaimé, F. Gustin, Review of characterization methods for supercapacitor modelling, J. Power Sources 246 (2014) 596–608.
[22] L. Changshi, Reliable and precise evaluation of energy-transfer and efficiency of supercapacitors, Renew. Sust. Energ. Rev. 151 (2021), 111566.
[23] L.M. Da Silva, R. Cesar, C.M.R. Moreira, J.H.M. Santos, L.G. De Souza, B.M. Pires, R. Vincentini, W. Nunes, H. Zanin, Reviewing the fundamentals of supercapacitors and the difficulties involving the analysis of the electrochemical findings obtained for porous electrode materials, Energy Storage Mater. 27 (2020) 555–590.
[24] H. Yang, A comparative study of supercapacitor capacitance characterization methods, J. Energy Storage 29 (2020), 101316.
[25] Y. Ge, X. Xie, J. Roscher, R. Holze, Q. Qu, How to measure and report the capacity of electrochemical double layers, supercapacitors, and their electrode materials, J. Solid State Electrochem. 24 (2020) 3215–3230.
[26] L.E. Helseth, Comparison of methods for finding the capacitance of a supercapacitor, J. Energy Storage 35 (2021), 102304.
[27] R. He, K.J. Aoki, J. Chen, Electric field-dependence of double layer capacitances by current-controlled charge-discharge steps, Electrochem 1 (2020) 217–225.
[28] I.V. Esarev, D.V. Agafonov, Y.V. Surovikin, S.N. Nesov, A.V. Lavrenov, On the causes of non-linearity of galvanostatic charge curves of electrical double layer capacitors, Electrochim. Acta 390 (2021), 138896.
[29] F. Licht, M.A. Davis, H.A. Andreas, Charge redistribution and electrode history impact galvanostatic charging/discharging and associated figures of merit, J. Power Sources 446 (2020), 227354.
[30] Y. Gogotsi, R.M. Penner, Energy storage in nanomaterials – capacitive, pseudocapacitive, or battery-like, ACS Nano 12 (2018) 2081–2083.
[31] Y. Jiang, J. Liu, Definitions of pseudocapacitive materials: a brief review, in: Energy&Environmental Materials 2, 2019, pp. 30–37.
[32] L. Guan, L. Yu, G.Z. Chen, Capacitive and non-capacitive faradaic charge storage, Electrochim. Acta 206 (2016) 464–478.
[33] G.Z. Chen, Supercapacitor and supercapattery as emerging electrochemical energy stores, Int. Mat. Rev. 62 (2017) 173–202.
[34] M.Z. Iqbal, U. Aziz, Supercapattery: merging of battery-supercapacitor electrodes for hybrid energy storage devices, J. Energy Storage 46 (2022), 103823.
[35] H. Su, C. Lian, A. Gallegos, S. Deng, Y. Shang, H. Liu, J. Wu, Microscopic insights into the Faradaic reaction effects on the electric double layers, Chem. Eng. Sci. 215 (2020), 115452.
[36] R.J. Hunter, Introduction to Modern Colloid Science, 1st ed., Oxford Science Publications, 1993.
[37] M. Hahn, O. Barbieri, F.R. Campana, R. Kotz, R. Gallay, Carbon based double layer capacitors with aprotic electrolyte solutions: the possible role of intercalation/insertion processes, Appl. Phys. A Mater. Sci. Process. 82 (2006) 633–638.
[38] P.W. Ruch, M. Hahn, F. Rosciano, M. Holzapfel, H. Kaiser, W. Scheifele, B. Schmitt, P. Novak, R. Kotz, A. Wokaun, In situ X-ray diffraction of the intercalation of (C2H5)4N+ and BF4- into graphite from acetonitrile and propylene carbonate based supercapacitor electrolytes, Electrochim. Acta 53 (2007) 1074–1082.
[39] W. Schmickler, Interfacial electrochemistry, Oxford University Press, 1996.
[40] H. Gualous, D. Bouquain, A. Berthon, J.M. Kauffmann, Experimental study of supercapacitor serial resistance and capacitance variations with temperature, J. Power Sources 123 (2003) 86–93.
[41] S. Rajput, A. Kuperman, A. Yahalom, M. Averbukh, Studies on dynamic properties of ultracapacitors using infinite r-C chain equivalent circuit and reverse fourier transform, Energies 13 (2020) 4583.
[42] Y. Abetbool, S. Rajput, A. Yahalom, M. Averbukh, Comprehensive study on dynamic parameters of symmetric and asymmetric ultracapacitors, Electronics 8 (2019) 891.
[43] D. Xu, L. Zhang, B. Wang, G. Ma, Modeling of supercapacitor behavior with an improved two-branch equivalent circuit, IEEE Access 7 (2019) 26379–26390.
[44] C. Liu, Y. Wang, Z. Chen, Q. Ling, A variable capacitance based modeling and power capability predicting method for ultracapacitor, J. Power Sources 374 (2018) 121–133.
[45] B. Wang, C. Wang, Q. Hu, L. Zhang, Z. Wang, Modelling the dynamic self-discharge effects of supercapacitors using a controlled current source based ladder equivalent circuit, J. Energy Storage 30 (2020), 101473.
[46] Y. Zhao, W. Xie, Z. Fang, S. Liu, A parameters identification method of the equivalent circuit model of the supercapacitor cell module based on segmentation optimization, IEEE Access 8 (2020) 92895–92906.
[47] G. Navarro, J. Najera, J. Torres, M. Blanco, M. Santos, M. Lafoz, Development and experimental validation of a supercapacitor frequency domain model for industrial energy applications considering dynamic behavior at high frequencies, Energies 13 (2020) 1156.
[48] P. Saha, S. Dey, M. Khanra, Accurate estimation of state-of-charge of supercapacitor under uncertain leakage and open circuit voltage map, J. Power Sources 434 (2019), 226696.
[49] P. Saha, S. Dey, M. Khanra, Second-life applications of supercapacitors: effective capacitance prognoses and aging, J. Power Sources 496 (2021), 229824.
[50] P. Saha, V. Ramadesigan, M. Khanra, An experimental study on the effectiveness of conventional state-of-health diagnosis schemes for second-use supercapacitors, J. Energy Storage 42 (2021), 102968.
[51] S. Buller, E. Karden, D. Kok, R. Doncker, Modeling the dynamic behavior of supercapacitors using impedance spectroscopy, IEEE Trans. Ind. Appl. 38 (2002) 1622–1626.
[52] Y. Parvini, J.B. Siegel, A.G. Stefanopoulou, A. Vahidi, Supercapacitor electrical and thermal modeling, identification, and validation for a wide range of temperature and power applications, IEEE Trans. Ind. Electron. 63 (2016) 1574–1585.
[53] I.N. Jiya, N. Gurusinghe, R. Gouws, Electrical circuit modelling of double layer capacitors for power electronics and energy storage applications: a review, Electronics 7 (2018) 268.
[54] L.E. Helseth, Modelling supercapacitors using a dynamic equivalent circuit with a distribution of relaxation times, J. Energy Storage 25 (2019), 100912.
[55] S. Satpathy, M. Dhar, B.K. Bhattacharyya, An integration of the review of electrode's materials and a new gamma function-based charging methodology of supercapacitor for high current applications, Mater. Today: Proc. 26 (2020) 2151–2156.
[56] L. Zubieta, R. Bonert, Characterization of double-layer capacitors for power electronics applications, IEEE Trans. Ind. Appl. 36 (2000) 199–205.
[57] H. Zhang, Y. Zhang, Estimation of supercapacitor energy using a linear capacitance for applications in wireless sensor networks, J. Power Sources 275 (2015) 498–505.
[58] H. Yang, Y. Zhang, Characterization of supercapacitor models for analyzing supercapacitors connected to constant power elements, J. Power Sources 312 (2016) 165–171.
[59] A. Oukaour, B. Tala-Ighil, M. AlSakka, H. Gualous, R. Gallay, B. Boudart, Calendar ageing and health diagnosis of supercapacitor, Electr. Power Syst. Res. 95 (2013) 330–338.
[60] R. Faranda, A new parameters identification procedure for simplified double layer capacitor two-branch model, Electr. Pow. Syst. Res. 80 (2010) 363–371.
[61] A.P.R. Fernandez, E.A. Périgo, R.N. Faria, Analytical expressions for electrochemical supercapacitor with potential dependent capacitance, J. Energy Storage 43 (2021), 103156.
[62] A.P.R. Fernandez, E.A. Perigo, R.N. Faria, Simulation of galvanostatic charge-discharge curves of carbon-based symmetrical electrochemical supercapacitor with organic electrolyte employing potential dependent capacitance and time domain analytical expression, J. Energy Storage 51 (2022), 104471.
[63] R. Vicentini, L.M. Da Silva, E.P.C. Junior, T.A. Alves, W.G. Nunes, H. Zanin, How to measure and calculate equivalent series resistance of electrical double layer capacitors, Molecules 24 (2019) 1452.
[64] M. Tokita, N. Yoshimoto, K. Fujii, M. Morita, Degradation characteristics of electric double-layer capacitors consisting of high surface area carbon electrodes with organic electrolyte solutions, Electrochim. Acta 209 (2016) 210–218.
[65] V. Ruiz, S. Roldan, I. Villar, C. Blanco, R. Santamaria, Voltage dependence of carbon-based supercapacitors for pseudocapacitance quantification, Electrochim. Acta 95 (2013) 225–229.
[66] P. Kurzweil, J. Schottenbauer, C. Schnell, Past, present and future of electrochemical capacitors: pseudocapacitance, aging mechanisms and service life estimation, J. Energy Storage 35 (2021), 102311.
[67] L.I. Dhaikin, A.A. Kornyshev, M. Urbakh, Double layer capacitance on a rough metal surface: surface roughness measured by 'Debye ruler', Electrochim. Acta 42 (1997) 2853–2860.
[68] L. Zeng, T. Wu, T. Ye, T. Mo, R. Qiao, G. Feng, Modeling galvanostatic charge-discharge of nanoporous supercapacitors, Nat. Comput. Sci. 1 (2021) 725–731.
[69] C. Pean, B. Rotenberg, P. Simon, M. Salanne, Multi-scale modelling of supercapacitors: from molecular simulations to a transmission line model, J. Power Sources 326 (2016) 680–685.
[70] Y. Bu, H. Liang, R. Shi, H. Liu, Y. Zhang, T. Sun, C. Lian, X. Shen, H. Li, Assessing the maximum power and consistency of carbon supercapacitors through a facile practical strategy, ACS Sustain. Chem. Eng. 8 (2020) 12430–12436.
[71] L.E. Helseth, The self-discharging of supercapacitors interpreted in terms of a distribution of rate constants, J. Energy Storage 34 (2021), 102199.
[72] V. Romano, B. Martin-Garcia, S. Bellani, L. Marasco, J.K. Panda, R. Oropesa-Nunez, L. Najafi, A.E. Del Rio Castillo, M. Prato, E. Mantero, V. Pellegrini, G. D'Angelo, F. Bonaccorso, Flexible graphene/carbon nanotube electrochemical double-layer capacitors with ultrahigh areal performance, ChemPlusChem 84 (2019) 882–892.
[73] P. Sivaraman, S.P. Mishra, D.D. Potphode, A.P. Thakur, K. Shashidhara, A. B. Samui, A.R. Bhattacharyya, A supercapacitor based on longitudinal unzipping of multi-walled carbon nanotubes for high temperature application, RSC Adv. 5 (2015) 83546.
[74] R. Vellacheri, A. Al-Haddad, H. Zhao, W. Wang, C. Wang, Y. Lei, High performance supercapacitor for efficient energy storage under extreme environmental temperatures, Nano Energy 8 (2014) 231–237.
[75] C. Zequine, C.K. Ranaweera, Z. Wang, S. Singh, P. Tripathi, O.N. Srivastava, B. K. Guptam, K. Ramasamy, P.K. Kahol, P.R. Dvornic, R.K. Gupta, High performance and flexible supercapacitors based on carbonized bamboo fibers for wide temperature applications, Scientific Reports 6 (2016) 31704.

[76] M. Morita, Y. Noguchi, M. Tokita, N. Yoshimoto, K. Fujii, T. Utsonomiya, Influences of residual water in high specific surface area carbon on the capacitor performances in an organic electrolyte solution, Electrochim. Acta 206 (2016) 427–431.
[77] Y. Liu, X. Qu, G. Huang, B. Xing, Y. Fan, C. Zhang, Y. Cao, Microporous carbon derived from anthracite as supercapacitor electrodes with commercial mass loading, J. Energy Storage 43 (2021), 103200.
[78] O. Bohlen, J. Kowal, D.U. Sauer, Ageing behaviour of electrochemical double layer capacitors. Part I. Experimental study and ageing model, J. Power Sources 172 (2007) 468–475.
[79] A. Oz, D. Gelman, E. Goren, N. Shomrat, S. Baltianski, Y. Tsur, A novel approach for supercapacitors degradation characterization, J. Power Sources 355 (2017) 74–82.
[80] D. Torregrossa, M. Paolone, Modelling of current and temperature effects on supercapacitors ageing. Part II: state of health assessment, J. Energy Storage 5 (2016) 95–101.
[81] T. Tevi, H. Yaghoubi, J. Wang, A. Takshi, Application of poly(p-phenylene oxide) as a blocking layer to reduce self-discharge in supercapacitors, J. Power Sources 241 (2013) 589–596.
[82] T. Tevi, A. Takshi, Modeling and simulation study of the self-discharge in supercapacitors in presence of a blocking layer, J. Power Sources 273 (2015) 857–862.
[83] S. Hamedi, T. Ghanbari, E. Moshksar, Z. Hosseini, Time-varying model of self-discharge in a double layer supercapacitor with blocking layer, J. Energy Storage 40 (2021), 102730.
[84] B.E. Conway, W.G. Pell, T.C. Liu, Diagnostic analyses for mechanisms of self-discharge of electrochemical capacitors and batteries, J. Power Sources 65 (1997) 53–59.
[85] B.W. Ricketts, C. Thon-That, Self-discharge of carbon-based supercapacitors with organic electrolytes, J. Power Sources 89 (2000) 64–69.
[86] M. Kaus, J. Kowal, D.U. Sauer, Modelling the effects of charge redistribution during self-discharge of supercapacitors, Electrochim. Acta 55 (2010) 7516–7523.
[87] J. Kowal, E. Avaroglu, F. Chamekh, A. Seinfelds, T. Thien, D. Wijaya, D.U. Sauer, Detailed analysis of the self-discharge of supercapacitors, J. Power Sources 196 (2011) 573–579.
[88] P. Kurzweil, M. Shamonin, State-of-charge monitoring by impedance spectroscopy during long-term self-discharge of supercapacitors and lithium-ion batteries, Batteries 4 (2018) 35.
[89] J. Black, H.A. Andreas, Effects of charge redistribution on self-discharge of electrochemical capacitors, Electrochim. Acta 54 (2009) 3568–3574.
[90] J. Black, H.A. Andreas, Predictions of the self-discharge profile of an electrochemical capacitor electrode in the presence of both activation-controlled discharge and charge redistribution, J. Power Sources 195 (2010) 929–935.
[91] A.M. Oickle, J. Tom, H.A. Andreas, Chemical oxidation and its influence on self-discharge in aqueous electrochemical capacitors, Carbon 110 (2016) 232–242.
[92] J.W. Graydon, M. Panjehshahi, D.W. Kirk, Charge redistribution and ionic mobility in the micropores of supercapacitors, J. Power Sources 245 (2014) 822–829.
[93] V. Sedlakova, J. Sikula, J. Mazner, P. Sedlak, T. Kuparowitz, B. Buergler, P. Vasina, Supercapacitor equivalent circuit model based on charges redistribution by diffusion, J. Power Sources 286 (2015) 58–65.
[94] R. de Fazio, D. Cafagna, G. Marcuccio, P. Visconti, Limitations and characterization of energy storage devices for harvesting applications, Energies 13 (2020) 783.
[95] Y. Wu, R. Holze, Self-discharge in supercapacitors: causes, effects and therapies: an overview, Electrochem. Energy Technol. 7 (2021) 1–37.
[96] H.A. Andreas, Self-discharge in electrochemical capacitors: a perspective article, J. Electrochem. Soc. 162 (2015) A5047–A5053.
[97] S. Satpathy, M. Dhar, B.K. Bhattacharyya, Why supercapacitor follows complex time-dependent power law and does not obey normal exponential rule, J. Energy Storage 31 (2020), 101606.
[98] S. Sahoo, P. Pazhamalai, V.K. Mariappan, G.K. Veerasubramani, N.J. Kim, S. J. Kim, Hydrothermally synthesized chalcopyrite platelets as an electrode material for symmetric supercapacitors, Inorg. Chem. Front. 7 (2020) 1492–1502.
[99] W.G. Pell, B.E. Conway, N. Marincic, Analysis of non-uniform charge/discharge and rate effects in porous carbon capacitors containing sub-optimal electrolyte concentrations, J. Electroanal. Chem. 491 (2000) 9–21.
[100] S. Jiang, T. Shi, X. Zhan, Y. Huang, Z. Tang, Superior electrochemical performance of carbon cloth electrode-based supercapacitors through surface activation and nitrogen doping, Ionics 22 (2016) 1881–1890.
[101] R.K. Jain, H.C. Gaur, B.J. Welch, Chronopotentiometry: a review of theoretical principles, J. Electroanal. Chem. 79 (1977) 211–236.